A&A, 708, A243 (2026)
https://doi.org/10.1051/0004-6361/202557147

Astronomy & Astrophysics

Towards an application of fourth-order shear statistics

I. The information content of $\langle M_{\rm ap}^4 \rangle$

Elena Silvestre-Rosello[1,2,⋆], Lucas Porth[2], Peter Schneider[2], Laila Linke[1], Jonas Krueger[1], Sebastian Grandis[1], and Jonathan Oel[3,2]

[1] Universität Innsbruck, Institut für Astro- und Teilchenphysik, Technikerstr. 25/8, 6020 Innsbruck, Austria
[2] University of Bonn, Argelander-Institut für Astronomie, Auf dem Hügel 71, 53121 Bonn, Germany
[3] Astronomy Centre, Department of Physics and Astronomy, University of Sussex, Brighton BN1 9RH, UK

Received 8 September 2025 / Accepted 16 December 2025

ABSTRACT

Context. Higher-order shear statistics contain part of the non-Gaussian information of the projected matter field and can therefore provide additional constraints on the cosmological parameters when combined with second-order statistics.
Aims. We aim to provide the theoretical framework for studying shear four-point correlation functions (4PCF) using fourth-order aperture statistics and develop a numerical integration pipeline to compute them. Finally, we aim to forecast the information content of fourth-order aperture statistics.
Methods. We began by giving the relation of the n-th order aperture statistics, $\langle M_{\rm ap}^n \rangle$, to the shear nPCF and to the convergence polyspectra. We then focused on the fourth-order case, where we derived the functional form of their filters and tested the behavior of these filters by numerically integrating over the 4PCF of a Gaussian random shear field (GRF). Finally, we performed a Fisher forecast on the constraining power of $\langle M_{\rm ap}^4 \rangle_{\rm c}$, where we developed a novel method to estimate derivatives from a simulation suite with arbitrarily distributed cosmological sets.
Results. By analyzing and mitigating numerical effects within the integration pipeline, we achieve a two-percent-level precision on the fourth-order aperture statistics for a GRF, which remains well below the noise budget of Stage IV surveys. We report a minimal improvement in the constraining power of the aperture statistics when including fourth-order statistics to a $\langle M_{\rm ap}^2 \rangle + \langle M_{\rm ap}^3 \rangle$ joint analysis for a DES-Y3-like setup, using non-tomographic equal-scale aperture statistics.

Key words. gravitational lensing: weak – methods: analytical – methods: numerical – large-scale structure of Universe

1. Introduction

For the past few decades, cosmic shear has provided insights into the contents and structure of the large-scale structure (LSS) of the Universe. Second-order shear statistics, which capture the Gaussian information in the field, have been key in constraining the cosmological parameters. The results for Stage III surveys can be found in Amon et al. (2022) and Secco et al. (2022) for the Dark Energy Survey, DES-Y3, Wright et al. (2025) and Stölzner et al. (2025) for the Kilo Degree Survey, KiDS Legacy, or Dalal et al. (2023) and Li et al. (2023) for the Hyper Suprime-Cam, HSC. As the observational precision increases, the significance of three-point statistics and other higher-order statistics also grows, successfully targeting the non-Gaussianities in the matter field, as forecasted by Euclid Collaboration: Ajani et al. (2023) on a *Euclid* setup (Euclid Collaboration: Mellier et al. 2025). In Stage III surveys, both two- and three-point shear statistics have been explored, as their joint analysis yields tighter constraints on the cosmological parameters than either can provide individually, as shown in Burger et al. (2024) for a joint analysis using the KiDS (Kuijken et al. 2015).

The exceptional precision of Stage IV surveys, such as *Euclid*, will give high signal-to-noise ratio (S/N) to statistics beyond third order (Euclid Collaboration: Ajani et al. 2023). This work is part of a two-part study, in which we explore fourth-order shear statistics and work toward their application.

Fourth-order statistics may break degeneracies between second- and third-order statistics, and therefore give tighter constraints on the cosmological parameters. Alternatively, they may be degenerate with the previous orders, in which case they present a new test for systematics and for the study of nuisance parameters, such as intrinsic alignment or baryonic models. Both scenarios can be relevant for Stage IV surveys, where second- and higher-order statistics will become standard tools for cosmology.

We began with a theoretical analysis on n-th order aperture statistics – extending prior work on second-order (Schneider et al. 2002) and third-order (Schneider et al. 2005; Heydenreich et al. 2023) formulations – and their connection to n-point polyspectra and n-point correlation functions (nPCFs). We then specialized to the fourth-order case, and derived the relation between fourth-order aperture statistics and the four-point correlation functions (4PCFs) of the shear field. Aperture statistics decompose the shear field into E- and B-modes, thus enabling robust detection of systematic errors. When computed via nPCFs, the aperture statistics are less sensitive to finite-field effects and masking biases (Jarvis et al. 2004; Schneider et al. 2005; Porth et al. 2020). However, the numerical transformations between nPCFs and aperture statistics can introduce small biases, which we studied and mitigated.

⋆ Corresponding author: elena.silvestre-rosello@uibk.ac.at

The companion paper, (Porth et al. 2025, hereinafter P25), presents an efficient estimator for the 4PCF based on a multipole decomposition, which computationally allows the measurement of fourth-order shear statistics. Building on the theoretical framework and computational pipelines established here, P25 report a significant detection of fourth-order aperture statistics using data from the first data release of the Dark Energy Survey (DES-Y3; Abbott et al. 2022).

Finally, we assess the incremental constraining power of including fourth-order statistics alongside second- and third-order aperture statistics. In particular, we evaluate the information content of the fourth-order statistics $\langle M_{\rm ap}^4 \rangle$ with a Fisher forecast on a DES-Y3-like setup.

The structure of this paper is as follows. In Sect. 2 we introduce the shear nPCF and the corresponding n-th order aperture statistics. Section 3 develops the fourth-order case analytically. In Sect. 4 we numerically compute the aperture statistics using a model for a Gaussian random field and assess the accuracy of the computation. Section 5 presents a Fisher forecast on the constraining power of fourth-order aperture statistics in a DES-Y3-like setup. We summarize and discuss the main results in Sect. 6.

2. Higher-order measures of cosmic shear

The fundamentals of weak lensing are described in Bartelmann & Schneider (2001). More recent cosmic shear descriptions can be found in Kilbinger (2015) and Mandelbaum (2018).

2.1. Basic concepts

In cosmology, the matter density field is usually characterized by the density contrast

$$\delta(\boldsymbol{X};\chi) = \frac{\rho_{\rm m}(\boldsymbol{X};\chi) - \bar{\rho}_{\rm m}(\chi)}{\bar{\rho}_{\rm m}(\chi)}, \tag{1}$$

with $\rho_{\rm m}(\boldsymbol{X};\chi)$ the three-dimensional matter density at an angular position, $\boldsymbol{X}$, and comoving distance, χ; and $\bar{\rho}_{\rm m}(\chi)$ its average value at a given χ.

The dimensionless surface mass density or convergence, $\kappa(\boldsymbol{X};\chi)$, is defined as the projection of the three-dimensional matter field along the line of sight from the observer until a given χ. For a flat universe it is given by

$$\kappa(\boldsymbol{X};\chi) = \frac{3H_0^2\Omega_{\rm m}}{2c^2} \times \int_0^{\chi} {\rm d}\chi' \frac{(\chi-\chi')\chi'}{\chi}\, \delta\left(\chi'\boldsymbol{X},\chi\right)\, [1+z(\chi')], \tag{2}$$

where H_0 is the Hubble constant, $\Omega_{\rm m}$ the matter density parameter, c the speed of light, and z the redshift, related to the comoving distance in the line of sight by ${\rm d}z\, c/H(z) = {\rm d}\chi$, with $H(z)$ the expansion rate of the Universe, from the first Friedmann equation (Friedmann 1922). In weak lensing, $\kappa(\boldsymbol{X};z)$ is a measure of the widening of light bundles at angular position $\boldsymbol{X}$ from sources at redshift z. If the sources follow a normalized redshift distribution, $p_z(z)$, which extends to a horizon redshift, $z_{\rm h}$, then

$$\kappa(\boldsymbol{X}) = \int_0^{z_{\rm h}} {\rm d}z\; p_z(z)\, \kappa(\boldsymbol{X};z). \tag{3}$$

The shear $\gamma_{\rm cart}(\boldsymbol{X};z)$ accounts for the distortion of such light bundles. It can be expressed as a complex number with respect to a reference direction or projection, described by the angle ζ_i with respect to the Cartesian axis; for a given redshift

$$\gamma(\boldsymbol{X};\zeta_i) = -\gamma_{\rm cart}(\boldsymbol{X}){\rm e}^{-2{\rm i}\zeta_i} = \gamma_{\rm t}(\boldsymbol{X};\zeta_i) + {\rm i}\gamma_\times(\boldsymbol{X};\zeta_i), \tag{4}$$

where we further decomposed the shear into its tangential and cross components, the value of which is projection dependent. Convergence and shear are related in Fourier space through

$$\hat{\gamma}(\boldsymbol{\ell}) = \hat{\kappa}(\boldsymbol{\ell}){\rm e}^{2{\rm i}\beta} \text{ and } \hat{\gamma}^*(\boldsymbol{\ell}) = \hat{\kappa}^*(\boldsymbol{\ell}){\rm e}^{-2{\rm i}\beta} = \hat{\kappa}(-\boldsymbol{\ell}){\rm e}^{-2{\rm i}\beta}, \tag{5}$$

with β the polar angle of $\boldsymbol{\ell}$, as in Kaiser & Squires (1993).

2.2. Convergence n-point polyspectra and shear n-point correlation functions

The n-point correlation function of the convergence (κnPCF) describes the statistical correlation of the convergence field as a function of the angular distribution of n points, and is defined as $\left\langle \prod_{i=0}^{n-1} \kappa(\boldsymbol{X}_i) \right\rangle$. It is related to the n-point polyspectrum $\mathcal{P}_{\kappa,n}$ through the Fourier transform of the convergence, $\hat{\kappa}(\boldsymbol{\ell})$,

$$\left\langle \prod_{i=1}^{n} \hat{\kappa}(\boldsymbol{\ell}_i) \right\rangle = (2\pi)^2\, \mathcal{P}_{\kappa,n}(\boldsymbol{\ell}_1,\cdots,\boldsymbol{\ell}_n)\, \delta_{\rm D}\left(\sum_{i=1}^{n} \boldsymbol{\ell}_i \right). \tag{6}$$

Following Eqs. (2) and (3), $\mathcal{P}_{\kappa,n}$ is a projection of the matter n-point polyspectrum $\mathcal{P}_{\delta,n}$ with the weighting function

$$g(z) = \chi(z) \int_z^{z_{\rm h}} {\rm d}z_{\rm s}\; p_z(z_{\rm s}) \frac{\chi(z_{\rm s}) - \chi(z)}{\chi(z_{\rm s})}, \tag{7}$$

which accounts for the lensing efficiency of lenses at redshift z[1]. The projected polyspectrum then reads, under the Limber and flat-sky approximations (Limber 1953),

$$\mathcal{P}_{\kappa,n}(\boldsymbol{\ell}_1,\cdots,\boldsymbol{\ell}_n) = \left(\frac{3H_0^2\Omega_{\rm m}}{2c^2}\right)^n \times \int_0^{z_{\rm h}} {\rm d}z \frac{g^n(z)\,(1+z)^n}{[\chi(z)]^{2(n-1)}} \mathcal{P}_{\delta,n}\left(\frac{\boldsymbol{\ell}_1}{\chi(z)},\cdots,\frac{\boldsymbol{\ell}_n}{\chi(z)}, z \right). \tag{8}$$

The lowest order polyspectra are commonly referred to as the power spectrum ($n = 2$), the bispectrum ($n = 3$), and the trispectrum ($n = 4$).

An n-point correlation function of shear (γnPCF or in the following simply nPCF) is defined as $\left\langle \prod_{i=0}^{n-1} \gamma^{(*)}(\boldsymbol{X}_i;\zeta_i) \right\rangle_p$, where p is the number of points with conjugated shear, without fixing any specific order. These are related to the polyspectra using Eqs. (5) and (6).

In order to compute an nPCF, the shear at every point $\boldsymbol{X}_i$ must be projected onto the direction determined by ζ_i, defining an nPCF projection $\pi \equiv \{\zeta_1,\cdots,\zeta_n\}$. For the two-point case the shear is projected onto the direction between the given points, so the 2PCF depends only on the separation θ between them. The 2PCF can be decomposed in the quantities $\xi_+(\theta)$, $\xi_-(\theta)$, and $\xi_\times(\theta)$, where the first two are related to the convergence power spectrum as described in Schneider et al. (2002) and the last one is expected to vanish due to parity invariance (Schneider 2003).

Generalizing the prescription outlined in Schneider & Lombardi (2003), the nPCF of a polar field, such as the shear field, consists of 2^{n-1} independent complex functions called the natural components $\Gamma_\mu^{\pi,n}$, $\mu = \{0,\cdots,2^{n-1}-1\}$.

[1] Some redshift information can be recovered by splitting the sources in tomographic bins with distinct $p_z(z_{\rm s})$.

The order of the different natural components is described in Appendix G.1 in P25, and specified for $n = 4$ in Sect. 3.1. For $n > 2$, the natural choice of projection π is not obvious and can lead to coordinate singularities. The study of the 4PCF is our main focus and is discussed further in Sect. 3.1.

2.3. Aperture statistics

The aperture mass statistics are a tool to decompose the shear field in its E- and B-modes by integrating the shear within a circular aperture of radius θ, centered at a position $\boldsymbol{\vartheta}$. The E-mode, or pure lensing signal, is contained in the aperture mass $M_{\rm ap}$ (Schneider 1996); while $M_\times$ quantifies the B-mode present in the field and can be used to estimate the mode-mixing due to higher-order and systematic effects (Schneider et al. 2002). Together they form the complex aperture measure

$$M(\boldsymbol{\vartheta};\theta) = M_{\rm ap}(\boldsymbol{\vartheta};\theta) + {\rm i}M_\times(\boldsymbol{\vartheta};\theta) \tag{9}$$

$$= \int {\rm d}\vartheta'\,\vartheta'\,Q_\theta(\vartheta') \int {\rm d}\zeta'\gamma(\boldsymbol{\vartheta}+\boldsymbol{\vartheta}';\zeta'), \tag{10}$$

with γ the shear and ζ the radial direction of $\boldsymbol{\vartheta}'$. The aperture mass $M_{\rm ap}$ can also be expressed as an integral over the convergence

$$M_{\rm ap}(\boldsymbol{\vartheta},\theta) = \int {\rm d}^2\,\vartheta'\,U_\theta(|\boldsymbol{\vartheta}-\boldsymbol{\vartheta}'|)\,\kappa(\boldsymbol{\vartheta}'), \tag{11}$$

with the compensated filter $U_\theta(|\boldsymbol{\vartheta}|)$ related with the filter $Q_\theta(|\boldsymbol{\vartheta}|)$ by

$$Q_\theta(\vartheta) = \frac{2}{\vartheta^2}\int_0^\vartheta {\rm d}\vartheta'\,\vartheta'\,U_\theta(\vartheta') - U_\theta(\vartheta). \tag{12}$$

Here we use the Gaussian filter by Crittenden et al. (2002),

$$Q_\theta(\vartheta) = \frac{\vartheta^2}{4\pi\theta^4}\exp-\frac{\vartheta^2}{2\theta^2}, \tag{13}$$

$$U_\theta(\vartheta) = \frac{1}{2\pi\theta^2}\left(1-\frac{\vartheta^2}{2\theta^2}\right)\exp-\frac{\vartheta^2}{2\theta^2}. \tag{14}$$

The moments of these complex aperture measures are the ensemble average of the product of apertures. The direct estimator for the moments, introduced by Schneider et al. (1998) for second-order moments and extended i.e. by Munshi & Coles (2003), computes the ensemble average as the average over all possible $N_{\rm a}$ aperture centers,

$$\left\langle M_{\rm ap}^n\right\rangle_{\rm dir}(\theta_1,\cdots,\theta_n) = \frac{\sum_i^{N_{\rm a}} M_{\rm ap}(\boldsymbol{\vartheta}_i,\theta_1)\cdots M_{\rm ap}(\boldsymbol{\vartheta}_i,\theta_n)}{N_{\rm a}}, \tag{15}$$

where the individual aperture masses are computed from Eq. (10) or Eq. (11). This estimator is biased when computed on masked fields, presents E- and B-mode mixing on finite fields (Heydenreich et al. 2023), and requires the subtraction of multiple-counting terms (Porth & Smith 2021).

The moments of the complex apertures can also be expressed as integrals of the shear correlators over the $(2n)$-dimensional configuration space. For an nPCF with p conjugated shears, where the shears are conjugated in the first p positions,

$$\langle (M^*)^p\ M^{n-p}\rangle(\theta_1,\cdots,\theta_n) = (-1)^n\int {\rm d}^2X_1\cdots\int {\rm d}^2X_n$$
$$\times\left(\prod_{i=1}^p Q_{\theta_i}(|\boldsymbol{X}_i|)\frac{\check{X}_i}{|\check{X}_i|}\right)\left(\prod_{j=p+1}^n Q_{\theta_j}(|\boldsymbol{X}_j|)\frac{\check{X}_j^*}{|\check{X}_j|}\right)$$
$$\times\left\langle\prod_{i=1}^p\gamma_{\rm cart}^*(\boldsymbol{X}_i)\prod_{j=p+1}^n\gamma_{\rm cart}(\boldsymbol{X}_j)\right\rangle, \tag{16}$$

where $\check{X}_i$ is the complex representation of the vector $\boldsymbol{X}_i$. Equivalent expressions can be obtained for the nPCF with the p conjugated shears in different positions. The shear correlator can be expressed in terms of the natural components of the nPCF, in which case we find 2^{n-1} distinct integrals, that are not affected by masks in the fields (Jarvis et al. 2004; Schneider et al. 2005; Porth et al. 2020). In Appendix A we derive the expressions for the filters for equal-scale aperture radii (A.1), the generalization to multi-scale aperture radii (A.2), and the separation into E- and B-modes (A.3).

Alternatively, $\left\langle M_{\rm ap}^n\right\rangle$ can be expressed as an integral in Fourier space over the n-point polyspectrum,

$$\left\langle M_{\rm ap}^n\right\rangle(\theta_1,\cdots,\theta_n) = \int\frac{{\rm d}^2l_1}{(2\pi)^2}\cdots\int\frac{{\rm d}^2l_{n-1}}{(2\pi)^2}\left(\prod_{i=1}^{n-1}[\hat{u}(\theta_i|\boldsymbol{\ell}_i|)]\right)$$
$$\times\ \hat{u}\left(\theta_n\left|\sum_{i=1}^{n-1}\boldsymbol{\ell}_i\right|\right)\mathcal{P}_{\kappa,n}\left(\boldsymbol{\ell}_1,\cdots,\boldsymbol{\ell}_{n-1},-\sum_{i=1}^{n-1}\boldsymbol{\ell}_i\right), \tag{17}$$

where we used Eq. (6) and $\hat{u}(\theta l)$ is the Fourier transform of $U_\theta(\vartheta)$.

It is useful to further decompose the nPCF and the aperture statistics into their connected and disconnected part, where the connected part contains the additional information to the n-th order, and the disconnected part is a combination of the m-th orders, $m < n$ (Bernardeau et al. 2002). Due to the isotropy of space, $\left\langle M_{\rm ap}\right\rangle$ approaches zero, such that the aperture statistics for $n \in \{2,3\}$ only contain connected terms, and the ones for $n = 4$ only contain connected and Gaussian ($n = 2$) terms, as discussed in Sect. 4; see Porth & Smith (2021) for a discussion on higher-orders.

3. Fourth-order measures of cosmic shear

From now on, we focus on the 4PCF and the fourth-order aperture measures. First, we describe the natural components of the 4PCF and their projection, and then we derive the filters for their conversion into aperture statistics.

3.1. Natural components of the 4PCF

The shear 4PCF are

$$\left\langle\gamma^{(*)}(\boldsymbol{X}_0;\zeta_0)\,\gamma^{(*)}(\boldsymbol{X}_1;\zeta_1)\,\gamma^{(*)}(\boldsymbol{X}_2;\zeta_2)\,\gamma^{(*)}(\boldsymbol{X}_3;\zeta_3)\right\rangle_p, \tag{18}$$

where the shear on each point can be either conjugated or not, i.e. $\gamma^*(\boldsymbol{X}_i;\zeta_i) = [\gamma_{\rm t}(\boldsymbol{X}_i;\zeta_i) - {\rm i}\gamma_\times(\boldsymbol{X}_i;\zeta_i)]$. We define the natural components of the shear 4PCF similarly to Schneider & Lombardi (2003), where for notational simplicity we drop the index related to the fourth-order and the redshift dependency,

$$\Gamma_0^{\rm cart}(\boldsymbol{X}_0,\boldsymbol{X}_1,\boldsymbol{X}_2,\boldsymbol{X}_3) = \langle\gamma_{\rm cart}(\boldsymbol{X}_0)\gamma_{\rm cart}(\boldsymbol{X}_1)\gamma_{\rm cart}(\boldsymbol{X}_2)\gamma_{\rm cart}(\boldsymbol{X}_3)\rangle, \tag{19}$$

where 'cart' represents the projection onto the Cartesian axis. The other natural components read, with the same components as $\Gamma_0^{\rm cart}$,

$$\begin{aligned}
&\Gamma_1^{\rm cart} = \langle\gamma^*\gamma\gamma\gamma\rangle, \quad \Gamma_2^{\rm cart} = \langle\gamma\gamma^*\gamma\gamma\rangle, \quad \Gamma_3^{\rm cart} = \langle\gamma\gamma\gamma^*\gamma\rangle,\\
&\Gamma_4^{\rm cart} = \langle\gamma\gamma\gamma\gamma^*\rangle, \quad \Gamma_5^{\rm cart} = \langle\gamma^*\gamma^*\gamma\gamma\rangle, \quad \Gamma_6^{\rm cart} = \langle\gamma^*\gamma\gamma^*\gamma\rangle,\\
&\Gamma_7^{\rm cart} = \langle\gamma^*\gamma\gamma\gamma^*\rangle.
\end{aligned} \tag{20}$$

The shear 4PCF in a projection π can be projected onto some other projection π' with the projection operator $P^{\pi,\pi'}$, for the different μ components,

$$\Gamma^{\pi'}_{\mu}(\boldsymbol{X}_0,\cdots,\boldsymbol{X}_3) = P^{\pi,\pi'}_{\mu}(\boldsymbol{X}_0,\cdots,\boldsymbol{X}_3)\,\Gamma^{\pi}_{\mu}(\boldsymbol{X}_0,\cdots,\boldsymbol{X}_3). \tag{21}$$

Owing to the homogeneity and isotropy of space, for a projection tied to the relative position of the four points, $\Gamma^{\pi}_{\mu}(\boldsymbol{X}_0,\boldsymbol{X}_1,\boldsymbol{X}_2,\boldsymbol{X}_3) = \Gamma^{\pi}_{\mu}(\vartheta_1,\vartheta_2,\vartheta_3,\psi_{12},\psi_{23})$, with ϑ_j the lengths from the vectors $\boldsymbol{\vartheta}_j = \boldsymbol{X}_j - \boldsymbol{X}_0$, $j = \{1,2,3\}$ (called radial coordinates hereinafter), and ψ_{12} and ψ_{23} the angles $\widehat{\boldsymbol{\vartheta}_1\boldsymbol{\vartheta}_2}$ and $\widehat{\boldsymbol{\vartheta}_2\boldsymbol{\vartheta}_3}$ (called angular coordinates), as defined in Fig. 1. Together the relative positions of the four points form a four-sided polygon or quadrilateral.

The center of mass of vertices (CMV) of such quadrilateral lies at the point that minimizes the distances to all vertices. The vectors from the CMV to a given vertex are

$$\boldsymbol{q}_0 = -\frac{\boldsymbol{\vartheta}_1+\boldsymbol{\vartheta}_2+\boldsymbol{\vartheta}_3}{4} \text{ and } \boldsymbol{q}_j = \boldsymbol{q}_0 + \boldsymbol{\vartheta}_j,\ j = \{1,2,3\}. \tag{22}$$

3.1.1. ×-projection of shear

Here we consider the ×-projection for the shear, adapted from Porth et al. (2024) and defined by the angles $\zeta^{\times}_j = \varphi_j$ for $j = \{1,2,3\}$ and $\zeta^{\times}_0 = (\varphi_1+\varphi_3)/2$ from Fig. 1. The projection operator for Γ_0 and Γ_1 from Cartesian coordinates are, in terms of the complex quantities $\breve{\vartheta}_j = |\boldsymbol{\vartheta}_j|(\cos\varphi_j + \mathrm{i}\sin\varphi_j)$,

$$P^{\times,\mathrm{cart}}_0(\boldsymbol{\vartheta}_1,\boldsymbol{\vartheta}_2,\boldsymbol{\vartheta}_3) = \mathrm{e}^{-2\mathrm{i}\sum_{j=0}^{3}\zeta^{\times}_j} = \mathrm{e}^{-\mathrm{i}(3\varphi_1+2\varphi_2+3\varphi_3)} \tag{23}$$

$$= \left(\frac{\breve{\vartheta}^*_1}{|\breve{\vartheta}_1|}\right)^3\left(\frac{\breve{\vartheta}^*_2}{|\breve{\vartheta}_2|}\right)^2\left(\frac{\breve{\vartheta}^*_3}{|\breve{\vartheta}_3|}\right)^3, \tag{24}$$

$$P^{\times,\mathrm{cart}}_1(\boldsymbol{\vartheta}_1,\boldsymbol{\vartheta}_2,\boldsymbol{\vartheta}_3) = \mathrm{e}^{-2\mathrm{i}\left(-\zeta^{\times}_0+\sum_{j=1}^{3}\zeta^{\times}_j\right)} = \mathrm{e}^{-\mathrm{i}(\varphi_1+2\varphi_2+\varphi_3)} \tag{25}$$

$$= \left(\frac{\breve{\vartheta}^*_1}{|\breve{\vartheta}_1|}\right)\left(\frac{\breve{\vartheta}^*_2}{|\breve{\vartheta}_2|}\right)^2\left(\frac{\breve{\vartheta}^*_3}{|\breve{\vartheta}_3|}\right), \tag{26}$$

and analogous for all other natural components.

This projection is used for the multipole-based nPCF estimator described in P25. Moreover, as shown in Sect. 4, the ×-projection also gives good results in transforming the 4PCF to the aperture measures. In practice, projecting means we replace the shear correlators in Eq. (16) by the product of $P^{\mathrm{cart},\times}_p$ and the nPCF in the ×-projection[2].

3.2. Fourth-order aperture statistics

We study the fourth-order aperture measures in the case of equal apertures, $\langle M^4\rangle(\theta)$, $\langle M^*M^3\rangle(\theta)$, and $\langle M^{*2}M^2\rangle(\theta)$, as Heydenreich et al. (2023) and Burger et al. (2024) showed that the equal aperture case contains most of the information for the combined second- and third-order aperture statistics.

3.2.1. Study of the filters for the 4PCF

The 4PCF depends on the relative positions of the four points $\boldsymbol{X}_i$, so the eight-dimensional integrals from Eq. (16) can be analytically reduced to five-dimensional ones by integrating over the position of the quadrilateral CMV and over the quadrilateral orientation φ_1; see Appendix B.1 for details.

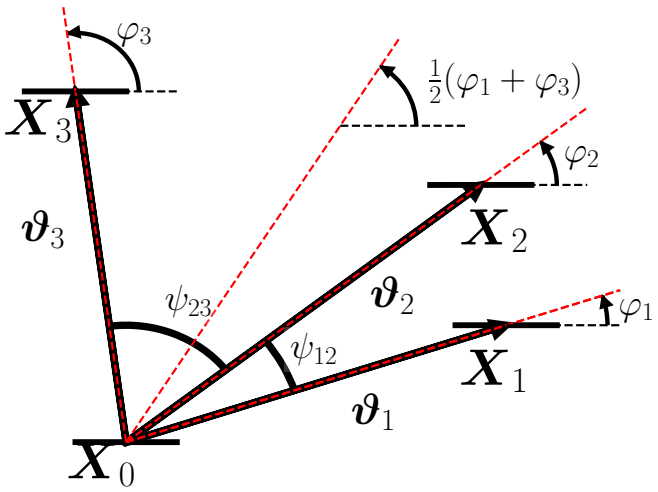

Fig. 1. Parametrization of a quadrilateral using the ×-projection. Equivalent to Fig. (1) from P25 by defining $\phi_{12} = \psi_{12}$ and $\phi_{13} = \psi_{12} + \psi_{23}$.

The apertures measures related to Γ_0, Γ_1 and Γ_5 read (and similarly for Γ_{2-4} and Γ_{6-7})

$$\begin{aligned}
\langle M^4\rangle(\theta) &= \prod_{j=1}^{3}\left(\int\frac{\mathrm{d}\vartheta_j}{\theta}\frac{\vartheta_j}{\theta}\right)\int\frac{\mathrm{d}\psi_{12}}{2\pi}\int\frac{\mathrm{d}\psi_{23}}{2\pi}\\
&\times K_0\left(\frac{\boldsymbol{q}_0}{\theta},\frac{\boldsymbol{q}_1}{\theta},\frac{\boldsymbol{q}_2}{\theta},\frac{\boldsymbol{q}_3}{\theta}\right)P^{\mathrm{cart},\times}_0\,\Gamma^{\times}_0(\vartheta_1,\vartheta_2,\vartheta_3,\psi_{12},\psi_{23}),\\
\langle M^*M^3\rangle(\theta) &= \prod_{j=1}^{3}\left(\int\frac{\mathrm{d}\vartheta_j}{\theta}\frac{\vartheta_j}{\theta}\right)\int\frac{\mathrm{d}\psi_{12}}{2\pi}\int\frac{\mathrm{d}\psi_{23}}{2\pi}\\
&\times K_1\left(\frac{\boldsymbol{q}_0}{\theta},\frac{\boldsymbol{q}_1}{\theta},\frac{\boldsymbol{q}_2}{\theta},\frac{\boldsymbol{q}_3}{\theta}\right)P^{\mathrm{cart},\times}_1\,\Gamma^{\times}_1(\vartheta_1,\vartheta_2,\vartheta_3,\psi_{12},\psi_{23}),\\
\langle M^{*2}M^2\rangle(\theta) &= \prod_{j=1}^{3}\left(\int\frac{\mathrm{d}\vartheta_j}{\theta}\frac{\vartheta_j}{\theta}\right)\int\frac{\mathrm{d}\psi_{12}}{2\pi}\int\frac{\mathrm{d}\psi_{23}}{2\pi}\\
&\times K_5\left(\frac{\boldsymbol{q}_0}{\theta},\frac{\boldsymbol{q}_1}{\theta},\frac{\boldsymbol{q}_2}{\theta},\frac{\boldsymbol{q}_3}{\theta}\right)P^{\mathrm{cart},\times}_5\,\Gamma^{\times}_5(\vartheta_1,\vartheta_2,\vartheta_3,\psi_{12},\psi_{23}),
\end{aligned} \tag{27}$$

where we defined the filter functions K_m, $m = \{0,\cdots,7\}$ in terms of the CMV vectors from Eq. (22)[3]. All dependencies of the filter on the aperture radius are through $\boldsymbol{\vartheta}/\theta$, so by defining $\boldsymbol{q}_{\mathrm{i}} = \boldsymbol{q}_i/\vartheta$,

$$K_0(\boldsymbol{q}_0,\cdots,\boldsymbol{q}_3) = \frac{1}{64}\prod_{i=0}^{3}\left(\breve{q}^{*2}_{\mathrm{i}}\,\exp-\frac{|\boldsymbol{q}_{\mathrm{i}}|^2}{2}\right), \tag{28}$$

$$\begin{aligned}
K_1(\boldsymbol{q}_0,\cdots,\boldsymbol{q}_3) = \frac{1}{64}\prod_{i=0}^{3}\left(\exp-\frac{|\boldsymbol{q}_{\mathrm{i}}|^2}{2}\right)\times\Big\{&\breve{q}^2_0\breve{q}^{*2}_1\breve{q}^{*2}_2\breve{q}^{*2}_3 +\\
&+2\breve{q}_0\left(\breve{q}^{*}_1\breve{q}^{*2}_2\breve{q}^{*2}_3 + 2\ \mathrm{cyclic}\right)+\\
&+\frac{1}{2}\left[\breve{q}^{*2}_1\left(\breve{q}^{*2}_2 + 4\breve{q}^{*}_2\breve{q}^{*}_3\right) + 2\ \mathrm{cyclic}\right]\Big\}
\end{aligned} \tag{29}$$

[2] A projection to the center of mass of vertices (CMV) was also considered, where the shear on the i-th vertex is projected onto the vector $\boldsymbol{q}_i$ from the CMV to said vertex. However, this projection is not used due to coordinate singularities for the filters when a quadrilateral vertex lies in the CMV.

[3] P25 use the projection-dependent filter functions

$$F^{(4,\times)}_{\mu}(\theta;\vartheta_1,\vartheta_2,\vartheta_3,\phi_{12},\phi_{13}) = K_{\mu}\left(\frac{\boldsymbol{q}_0}{\theta},\cdots,\frac{\boldsymbol{q}_3}{\theta}\right)P^{\mathrm{cart},\times}_{\mu}(\boldsymbol{\vartheta}_1,\boldsymbol{\vartheta}_2,\boldsymbol{\vartheta}_3),$$

with $\boldsymbol{q}_i$ from Eq. (22).

where the two terms correspond to a cyclic permutation of the indices one to three, and

$$K_5(\boldsymbol{\ell}_0,\cdots,\boldsymbol{\ell}_3) = \frac{1}{64}\left(\prod_{i=0}^{3}\exp-\frac{|\boldsymbol{\ell}_i|^2}{2}\right)\times\Big[\,\breve{\gamma}_0^2\breve{\gamma}_1^2\breve{\gamma}_2^{*2}\breve{\gamma}_3^{*2}+ \\ +2\breve{\gamma}_0\breve{\gamma}_1\breve{\gamma}_2^*\breve{\gamma}_3^*(\breve{\gamma}_0+\breve{\gamma}_1)\left(\breve{\gamma}_2^*+\breve{\gamma}_3^*\right)+ \\ +\frac{1}{2}\left(\breve{\gamma}_0^2+\breve{\gamma}_1^2+4\breve{\gamma}_0\breve{\gamma}_1\right)\left(\breve{\gamma}_2^{*2}+\breve{\gamma}_3^{*2}+4\breve{\gamma}_2^*\breve{\gamma}_3^*\right)+ \\ +3(\breve{\gamma}_0+\breve{\gamma}_1)\left(\breve{\gamma}_2^*+\breve{\gamma}_3^*\right)+\frac{3}{2}\Big]. \tag{30}$$

The filter functions for the other natural components can be obtained from the ones shown above by renaming the vertex with a conjugated shear, i.e.

$$\begin{aligned}
K_2(\breve{\gamma}_0,\breve{\gamma}_1,\breve{\gamma}_2,\breve{\gamma}_3) &= K_1(\breve{\gamma}_1,\breve{\gamma}_0,\breve{\gamma}_2,\breve{\gamma}_3),\\
K_3(\breve{\gamma}_0,\breve{\gamma}_1,\breve{\gamma}_2,\breve{\gamma}_3) &= K_1(\breve{\gamma}_2,\breve{\gamma}_1,\breve{\gamma}_0,\breve{\gamma}_3),\\
K_4(\breve{\gamma}_0,\breve{\gamma}_1,\breve{\gamma}_2,\breve{\gamma}_3) &= K_1(\breve{\gamma}_3,\breve{\gamma}_1,\breve{\gamma}_2,\breve{\gamma}_0),\\
K_6(\breve{\gamma}_0,\breve{\gamma}_1,\breve{\gamma}_2,\breve{\gamma}_3) &= K_5(\breve{\gamma}_0,\breve{\gamma}_2,\breve{\gamma}_1,\breve{\gamma}_3),\\
K_7(\breve{\gamma}_0,\breve{\gamma}_1,\breve{\gamma}_2,\breve{\gamma}_3) &= K_5(\breve{\gamma}_0,\breve{\gamma}_3,\breve{\gamma}_2,\breve{\gamma}_1).
\end{aligned} \tag{31}$$

These filters are equivalent to those in Jarvis et al. (2004), considering the notation change in the natural components. A cyclic permutation of indices as described there is equivalent to the vertex exchange due to the symmetry of the filters.

Appendix B.2 shows the dependency of the filters on the radial and angular coordinates. Due to their complicated profile, it is expected that the integration of the 4PCF over them requires some careful study, for which we refer to Sect. 4.

3.2.2. Aperture statistics from 4PCF

An E/B-mode separation is possible following the prescription in Appendix A.3, giving

$$\langle M_{\rm ap}^4\rangle = \frac{1}{8}\Re\left[(1,1,1,1,1,1,1,1)\cdot\mathcal{M}\right], \tag{32}$$

$$\langle M_{\rm ap}^3 M_\times\rangle = \frac{1}{8}\Im\left[\left(1,\frac{1}{2},\frac{1}{2},\frac{1}{2},\frac{1}{2},0,0,0\right)\cdot\mathcal{M}\right], \tag{33}$$

$$\langle M_{\rm ap}^2 M_\times^2\rangle = \frac{1}{8}\Re\left[\left(-1,0,0,0,0,\frac{1}{3},\frac{1}{3},\frac{1}{3}\right)\cdot\mathcal{M}\right], \tag{34}$$

$$\langle M_{\rm ap} M_\times^3\rangle = \frac{1}{8}\Im\left[\left(-1,\frac{1}{2},\frac{1}{2},\frac{1}{2},\frac{1}{2},0,0,0\right)\cdot\mathcal{M}\right], \tag{35}$$

$$\langle M_\times^4\rangle = \frac{1}{8}\Re\left[(1,-1,-1,-1,-1,1,1,1)\cdot\mathcal{M}\right], \tag{36}$$

with $\mathcal{M} = \big(\langle M^4\rangle,\langle M^*M^3\rangle,\langle MM^*M^2\rangle,\langle M^2M^*M\rangle,\langle M^3M^*\rangle,\langle M^{*2}M^2\rangle,\langle M^*MM^*M\rangle,\langle M^*M^2M^*\rangle\big)^{\rm T}$, where all measures depend on θ. The eight complex apertures measures are necessary for a decomposition of the fields in E- and B-modes in the presence of shape noise and tomographic measurements.

For a pure E-mode field, $\langle M_{\rm ap}^4\rangle$ is the only nonzero component, while $\langle M_{\rm ap}^2 M_\times^2\rangle$ are nonzero in the presence of E- and B-modes, and $\langle M_{\rm ap}^3 M_\times\rangle$ and $\langle M_{\rm ap} M_\times^3\rangle$ would be nonzero for a parity violating field (Schneider 2003).

While the E/B-decomposition described above is theoretically exact, it cannot be realized for a measurement of the shear 4PCF on real data, which are a noisy estimate of the bin-averaged 4PCF on a finite radial interval. We discuss the effects arising from the numerical integration in Sect. 4.

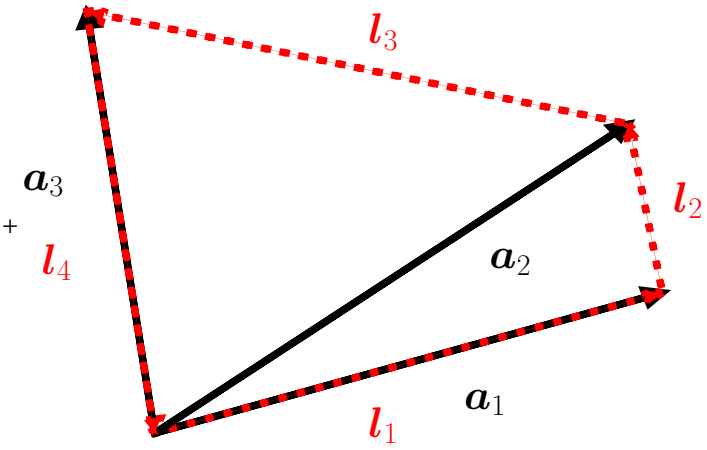

Fig. 2. Sketch of the two sets of coordinates for the projected trispectrum.

3.2.3. Aperture statistics from trispectrum

The fourth-order aperture mass can be obtained alternatively as an integral over the convergence trispectrum, specifying Eq. (17) to fourth order and equal-scale apertures,

$$\left\langle M_{\rm ap}^4\right\rangle(\theta) = \int\frac{{\rm d}^2 l_1}{(2\pi)^2}\cdots\int\frac{{\rm d}^2 l_3}{(2\pi)^2}\prod_{i=1}^{3}\left[\hat{u}(\theta|\boldsymbol{\ell}_i|)\right] \\ \times\hat{u}\left(\theta\left|\sum_{i=1}^{3}\boldsymbol{\ell}_i\right|\right)\mathcal{P}_{\kappa,4}\left(\boldsymbol{\ell}_1,\cdots,\boldsymbol{\ell}_3,-\sum_{i=1}^{3}\boldsymbol{\ell}_i\right). \tag{37}$$

In Fourier space, the vectors $\boldsymbol{\ell}_\alpha$, $\alpha=\{1,\cdots,4\}$, form a closed quadrilateral, ensured by the Delta function from Eq. (6). On the computational side, we find it more convenient to change the integration coordinates to the vectors $\{\boldsymbol{a}_1,\boldsymbol{a}_2,\boldsymbol{a}_3\}=\{\boldsymbol{\ell}_1,\boldsymbol{\ell}_1+\boldsymbol{\ell}_2,\boldsymbol{\ell}_1+\boldsymbol{\ell}_2+\boldsymbol{\ell}_3\}$ as defined in Fig. 2, where the closed quadrilateral condition is directly satisfied,

$$\begin{aligned}
\left\langle M_{\rm ap}^4\right\rangle(\theta) &= \int\frac{{\rm d}^2 a_1}{(2\pi)^2}\cdots\int\frac{{\rm d}^2 a_3}{(2\pi)^2} \\
&\quad\times\mathcal{P}_{\kappa,4}(\boldsymbol{a}_1,\boldsymbol{a}_2-\boldsymbol{a}_1,\boldsymbol{a}_3-\boldsymbol{a}_2,-\boldsymbol{a}_3) \\
&\quad\times\hat{u}(\theta|\boldsymbol{a}_1|)\,\hat{u}(\theta|\boldsymbol{a}_2-\boldsymbol{a}_1|)\,\hat{u}(\theta|\boldsymbol{a}_3-\boldsymbol{a}_2|)\,\hat{u}(\theta|-\boldsymbol{a}_3|) \\
&=8\int_{\mathbb{R}}\frac{{\rm d}a_1}{2\pi}\cdots\int_{\mathbb{R}}\frac{{\rm d}a_3}{2\pi}\int_0^{\pi}\frac{{\rm d}\alpha_{12}}{2\pi}\int_0^{\alpha_{12}}\frac{{\rm d}\alpha_{23}}{2\pi} \\
&\quad\times\mathcal{P}_{\kappa,4}(\boldsymbol{a}_1,\boldsymbol{a}_2-\boldsymbol{a}_1,\boldsymbol{a}_3-\boldsymbol{a}_2,-\boldsymbol{a}_3) \\
&\quad\times\hat{u}(\theta|\boldsymbol{a}_1|)\,\hat{u}(\theta|\boldsymbol{a}_2-\boldsymbol{a}_1|)\,\hat{u}(\theta|\boldsymbol{a}_3-\boldsymbol{a}_2|)\,\hat{u}(\theta|-\boldsymbol{a}_3|) \\
&\quad\times\left(1-\frac{\delta_{\rm D}(a_2-a_1)}{2}\right)\left(1-\frac{\delta_{\rm D}(a_3-a_2)}{2}\right) \\
&\quad\times\left(1-\frac{\delta_{\rm D}(a_1-a_3)\,[1-\delta_{\rm D}(a_2-a_1)]}{2}\right)
\end{aligned} \tag{38}$$

where in the second step we reduce the integration hypervolume by considering that the quadrilateral is symmetric under exchange $\alpha_{12}\to-\alpha_{12}$ and $\alpha_{12}\leftrightarrow\alpha_{23}$. The $\delta_{\rm D}$ factors avoid double counting in case two of the a_i have the same value, the last one accounting for $(a_1=a_2\ \&\ a_2=a_3)\implies(a_1=a_3)$.

However, we do not recommend this approach on observational data because the conversion from observable (real) space to Fourier space involves an integral over the whole real space, which is not practical due to finite survey sizes. Moreover, the integral over the nPCF is unaffected by masks in the field (Schneider et al. 2005; Jarvis et al. 2004).

4. Case of Gaussian random fields

We test the expressions for the aperture filters for the 4PCF, Eqs. (28)–(30), by assuming a Gaussian random shear field (GRF), which is chosen for three main reasons. Firstly, GRF are fully described by their second-order moments, i.e. their 2PCFs or their power spectrum. Therefore, for such fields, any $(2n)$-PCF can be written as a combination of 2PCFs, and any $(2n+1)$-PCF vanishes. In Appendix C.1 we explicitly show the form of the shear 4PCFs in terms of the shear 2PCFs for a GRF. Secondly, in this case the fourth-order aperture statistics can also be decomposed into second-order aperture statistics, as we discuss in Sect. 4.1. Finally, the shear field approaches, on large scales, a GRF, so on those scales the full 4PCF (connected and disconnected terms) is expected to behave similarly to that obtained from a realistic 2PCF, as seen in Fig. 3 from P25.

4.1. Fourth-order filters in terms of second-order filters

In Appendix C.2 we show the expressions for $\langle M^{(*)}M^{(*)}M^{(*)}M^{(*)}\rangle(\theta)$ as a function of $\langle MM\rangle(\theta)$ and $\langle MM^*\rangle(\theta)$ for the non-tomographic case and equal aperture scales. This allows us to relate the fourth- and second-order aperture statistics by using Eq. (10),

$$\langle M_{\rm ap}^4\rangle = 3\left[\langle M_{\rm ap}^2\rangle\right]^2, \tag{39}$$

$$\langle M_{\rm ap}^3 M_\times\rangle = 3\langle M_{\rm ap}M_\times\rangle\langle M_{\rm ap}^2\rangle, \tag{40}$$

$$\langle M_{\rm ap}^2 M_\times^2\rangle = \langle M_{\rm ap}^2\rangle\langle M_\times^2\rangle + 2\left[\langle M_{\rm ap}M_\times\rangle\right]^2, \tag{41}$$

$$\langle M_{\rm ap}M_\times^3\rangle = 3\langle M_{\rm ap}M_\times\rangle\langle M_\times^2\rangle, \tag{42}$$

$$\langle M_\times^4\rangle = 3\left[\langle M_\times^2\rangle\right]^2, \tag{43}$$

where all quantities depend on θ. For a general field, these describe the disconnected part of the fourth-order statistics, with $\langle M_{\rm ap}^4\rangle$ the only non-zero component for a pure E-mode field. Then, the connected aperture statistics can be obtained by subtracting Eqs. (39)–(43) from the general aperture statistics in Eqs. (32)–(36), as described in Sect. 5.3 in P25.

4.2. Integration routine

The integrals in Eq. (27) are numerically computed using a model for a Gaussian shear field. For that, the 2PCFs are obtained with `pyccl` (Chisari et al. 2019)[4], assuming a flat Λ cold dark matter cosmology with matter density $\Omega_{\rm m} = 0.30$, null baryonic and radiation density $\Omega_{\rm b} = 0.00 = \Omega_{\rm r}$, a reduced Hubble constant $h = 0.7$, $\sigma_8 = 0.8$, and spectral index $n_s = 0.96$. The shear field presents a Gaussian redshift distribution of mean $\bar{z} = 1.5$ and standard deviation $\sigma_z = 0.15$. The 4PCFs are obtained from the linearly interpolated 2PCFs using the prescription in Appendix C.1.

We estimate Eq. (27) using a Riemann sum with $N_{\rm ang}$ almost linearly spaced angular bins for ψ_{12} and ψ_{23}, and $N_{\rm rad}$ logarithmically spaced radial bins for ϑ_i (see Sect. 4.2.3 for a discussion on the geometry). The integral over the l-th natural component corresponds to the aperture measure $\left\langle M^{(*)4}\right\rangle_{\rm Rie}^l(\theta)$,

$$\left\langle M^{(*)4}\right\rangle_{\rm Rie}^l(\theta) = \sum_{i,j,k=1}^{N_{\rm rad}} \frac{\vartheta_i\Delta_{\vartheta;i}}{\theta^2}\frac{\vartheta_j\Delta_{\vartheta;j}}{\theta^2}\frac{\vartheta_k\Delta_{\vartheta;k}}{\theta^2} \times \sum_{m,n=1}^{N_{\rm ang}} \frac{\Delta_{\psi;m}}{2\pi}\frac{\Delta_{\psi;n}}{2\pi} K_l\left(\frac{\boldsymbol{q}_0}{\theta},\frac{\boldsymbol{q}_1}{\theta},\frac{\boldsymbol{q}_2}{\theta},\frac{\boldsymbol{q}_3}{\theta}\right) \times P_l^{\rm cart,\times}\Gamma_l^\times\left(\vartheta_i,\vartheta_j,\vartheta_k,\psi_{12;m},\psi_{23;n}\right), \tag{44}$$

where ϑ_i is the arithmetic center of the i-th radial bin of width $\Delta_{\vartheta;i}$[arcmin], $\psi_{12;m}$ is the arithmetic center of the m-th angular bin of width $\Delta_{\psi;m}$[rad] and similarly for the other coordinates. The vectors $\boldsymbol{q}_0$ to $\boldsymbol{q}_3$ are computed from Eq. (22) using the centers of the binned radial and angular components.

The complexity of this method scales as $N_{\rm ang}^2 N_{\rm rad}^3$, which is computationally expensive. Nonetheless, as we show in the following, this is not a serious concern, since the bottleneck in the application of fourth-order aperture statistics lies in the computation of the 4PCF, described in P25.

In order to assess the precision of the estimated fourth-order aperture statistics, $\left\langle M^{(*)4}\right\rangle_{\rm Rie}^l$, we compare the estimate for $\left\langle M_{\rm ap}^4\right\rangle$ from Eq. (32) with that of Eq. (39), with $\left\langle M_{\rm ap}^2\right\rangle$ computed from the 2PCF using the transformation equations, Eq. (32) of Schneider et al. (2002) and the second-order filters in Jarvis et al. (2004).

4.2.1. Bin geometry

We find that not all quadrilateral configurations contribute equally to the given aperture measure. Fig. 3 shows the integrand of Eq. (44) after the radial integration for apertures with radii $\theta \in \{2', 20'\}$, in terms of the two angles from Fig. 1. The integrand's one-dimensional angular profile is also shown in Fig. 3 as the projection onto the ψ_{12} axis.

Most of the weight in the integrals is in quadrilateral configurations where at least two points are close by and are "mixed pairs", i.e. only one of the points has conjugated shear, so the phase factor in Eqs. (C.3)–(C.5) is unity, an effect that is stronger for large aperture radii. The vertices with conjugated shear depend on the natural component over which we integrate. For Γ_1, for example, the conjugated shear is on the vertex at $\boldsymbol{X}_0$, so "mixed pairs" include such vertex and most power is around small ϑ_i, with low angular dependency. For the integrals with Γ_i, $i > 1$, we find "mixed pairs" around vertices that are not in the origin, so most of the power comes from under- and asymmetrically sampled regions around $\boldsymbol{X}_j$, $j = \{1, 2, 3\}$.

Due to the sharp peaks around the configurations with angles equal to zero, we choose an angular binning scheme that samples the angles ψ_{12}, ψ_{23}, and $(\psi_{12} + \psi_{23})$ symmetrically around 0 rad. This results in consistent underestimations for low binning accuracy, as seen in Sect. 4.2.3. Moreover, we find that the most consistent results are found when using hypercubical bins, where for each radial and angular coordinate $\vartheta\Delta_\psi \approx \Delta_\vartheta$, which in the limit of infinitesimally small bins $\Delta_\vartheta = \vartheta\Delta(\ln\vartheta)$ corresponds to $\Delta_\psi = \Delta(\ln\vartheta)$, i.e. logarithmically spaced radial bins.

4.2.2. Integration range effects

In a realistic case, the radial integration cannot extend over the entire domain due to a finite number density of sources and a finite survey extent.

On aperture radii $\theta \in [2', 20']$ an integration range $\vartheta \in [\vartheta_{\rm min}, \vartheta_{\rm max}] = [e^{-2}', e^5']$ gives a result consistent with expectations from second-order statistics on a few percent level, as shown in Fig. 4 for the preferred set of binning parameters discussed in Sect. 4.2.3. Here and in Figs. 5–6 we compute the relative difference with respect to a ground truth, estimated as

[4] https://github.com/LSSTDESC/CCL

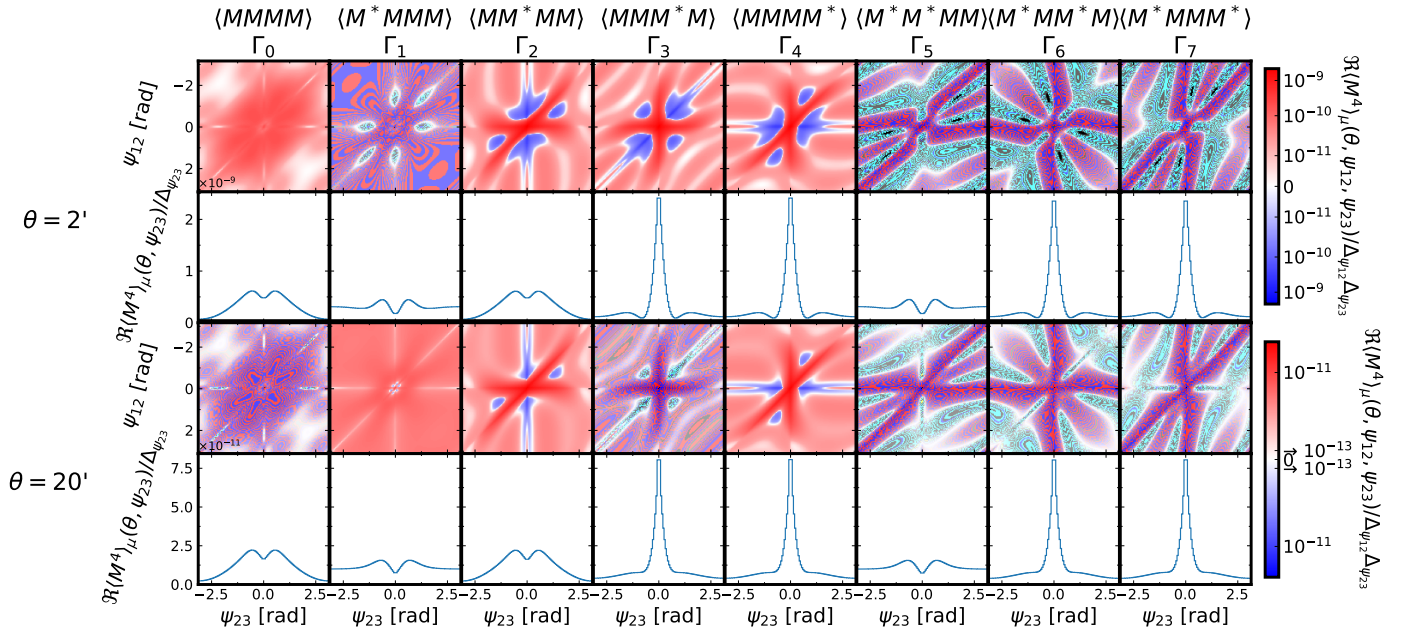

Fig. 3. Integrand for the eight complex aperture measures once the radial integration is performed (first and third rows) and once all but one angular integral are performed (second and fourth rows), computed on 126 radial bins and 113 angular bins. At small aperture radii, $\theta = 2'$ (top two rows), we find a higher signal, while at large aperture radii, $\theta = 20'$ (bottom two rows), the signal is more strongly peaked around the zero-angles. The peaks from the one-dimensional profiles correspond to close-by mixed-pair configurations, which play a stronger role for large θ, thus resulting in a smaller region of relative high values in the bottom rows. Similar peaks as in the integral over Γ_2, Γ_3, Γ_6, and Γ_7 can be found for the integral over Γ_4 and Γ_5 by projecting onto another angle (ψ_{23} or $\psi_{12}+\psi_{23}$). The integrals over Γ_0 and Γ_1 are smoother, so a faster convergence with binning accuracy is expected. The color bars are in `Symlog` scale (Hunter 2007), i.e. in logarithmic scale for large absolute values and linear scale for values around 0, with the linear threshold 170 times lower than the maximum for each aperture.

$3\left\langle M_{\rm ap}^2\right\rangle^2$, computed with integration range $\vartheta \in [\mathrm{e}^{-5}{}', \mathrm{e}^{9}{}']$ and a logarithmic bin width of $\Delta(\ln\vartheta) = 0.04$.

The discrepancy for small integration ranges is dominated by E-mode/B-mode mixing, arising from the impact of a finite integration range in the second-order aperture statistics described in Kilbinger et al. (2006). The dash-dotted lines in Fig. 4 show how these effects propagate into the Gaussian fourth-order statistics through Eqs. (39)–(43), when the integration range is too small, here $\vartheta \in [\mathrm{e}^{-2}{}', \mathrm{e}^{5}{}']$.

The behavior when $\left\langle M_{\rm ap}^4\right\rangle$ is estimated from the 4PCF with Eq. (32) differs because of our integration scheme, since the ϑ boundaries restrict the minimum and maximum separation between pairs that include the vertex $\boldsymbol{X}_0$, but the distances d between other vertices depend on the bin distribution[5]. On small scales the recovered B-mode is smaller than the one propagated from the 2PCF because, for some configurations, $d < \vartheta_{\rm min}$. On large scales the obtained B-mode is larger due to the finite size of the logarithmic bins, which sets $d > \vartheta_{\rm max}$ for large ϑ_i.

4.2.3. Binning accuracy

For a given integration range, the apparent convergence of the integral depends on the binning accuracy. Fig. 5 shows the convergence of the integrals for an increasing number of radial bins.

At large θ, the dispersion for different natural components arises, for a GRF, from the different weight given to quadrilateral configurations at large radii, where the bin size is large. The bottom panel in Fig. 5 shows that the largest underestimations are found for the integrals over Γ_μ with $\mu > 1$, as expected from Sect. 4.2.1.

[5] We added an artificial boundary of $d \in [10^{-3}{}', 10^{4}{}']$ on the 2PCF.

On scales $\theta \in [2', 20']$, using radial integration limits $\vartheta \in [\mathrm{e}^{-2}{}', \mathrm{e}^{5}{}']$, and a binning scheme with 87 angular bins and 98 radial bins, i.e. $\Delta(\ln\vartheta) = 0.07$, we obtained results that are within a two percent-level precision. On larger θ the precision increases to the percent level.

4.3. Integrated 4PCF

A realistic 4PCF cannot be evaluated at a fixed quadruplet configuration $(\vartheta_1, \vartheta_2, \vartheta_3, \psi_{12}, \psi_{23})$, since the probability of finding a quadruplet at such exact configuration is formally zero. The 4PCF is then averaged over all quadruplets in a radial bin, i.e. integrated over the radial grid of bin width $\Delta_{\vartheta;i}$, for the i-th bin

$$\overline{\Gamma}^{\times}_{\mu\,i,j,k,m,n} = \frac{1}{\Delta_{\vartheta;i}\Delta_{\vartheta;j}\Delta_{\vartheta;k}} \int_{\vartheta_{1;i}-0.5\Delta_{\vartheta;i}}^{\vartheta_{1;i}+0.5\Delta_{\vartheta;i}} \mathrm{d}\vartheta_1 \int_{\vartheta_{2;j}-0.5\Delta_{\vartheta;j}}^{\vartheta_{2;j}+0.5\Delta_{\vartheta;j}} \mathrm{d}\vartheta_2 \times \int_{\vartheta_{3;k}-0.5\Delta_{\vartheta;k}}^{\vartheta_{3;k}+0.5\Delta_{\vartheta;k}} \mathrm{d}\vartheta_3\, \Gamma^{\times}_{\mu}\left(\vartheta_1, \vartheta_2, \vartheta_3, \psi_{12;m}, \psi_{23;n}\right). \tag{45}$$

By using a multipole-based estimator (described in P25) we are free to choose the angular positions within a precision determined by the number of multipoles. The estimate of the aperture measure for the μ-th natural component reads

$$\left\langle M^{(*)4}\right\rangle^{\mu}_{\rm Rie,int}(\theta) = \sum_{i,j,k=1}^{N_{\rm rad}} \frac{\vartheta_i\Delta_{\vartheta;i}}{\theta^2}\frac{\vartheta_j\Delta_{\vartheta;j}}{\theta^2}\frac{\vartheta_k\Delta_{\vartheta;k}}{\theta^2} \times \sum_{m,n=1}^{N_{\rm ang}} \frac{\Delta_{\psi;m}}{2\pi}\frac{\Delta_{\psi;n}}{2\pi}\,\overline{\Gamma}^{\times}_{\mu\,i,j,k,m,n}\,K_{\mu;ijkmn}, \tag{46}$$

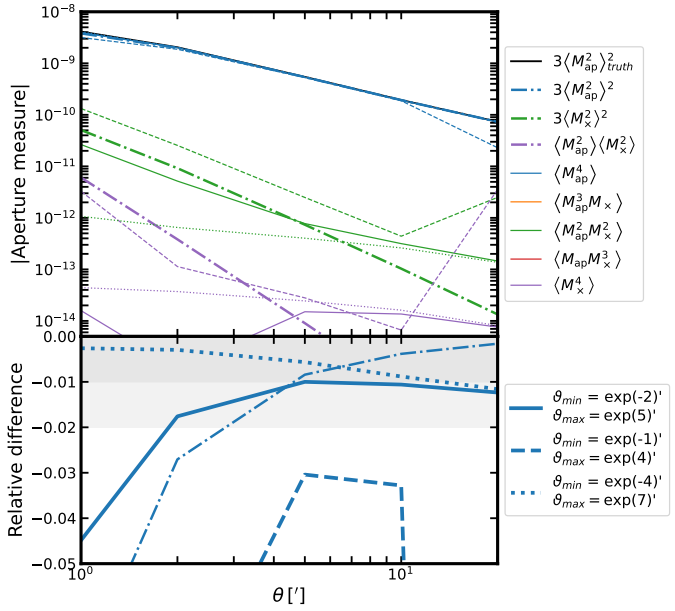

Fig. 4. Effect of a finite radial integration range on the fourth-order aperture statistics. (Top) Aperture statistics for varying radial integration ranges, computed on a grid with a logarithmic bin width of $\Delta(\ln\vartheta) = 0.07$ and $\Delta_\psi = 0.07$ rad alongside the considered ground truth (see text). Dash-dotted lines show the effect of E- and B-mode mixing in the second-order aperture statistics for a radial integration range $\vartheta \in [\mathrm{e}^{-2}{}', \mathrm{e}^{5}{}']$, propagated to the fourth-order with Eqs. (39)–(43). Parity violating modes are, in all cases considered here, below 10^{-20}. The discrepancies found on the pure B-mode arise from the combination of inaccurate complex aperture measures, and remain on all considered scales and cases smaller than 0.1% of the E-mode, thus well below noise levels for Stage III or Stage IV surveys. (Bottom) Relative difference for $\left\langle M_{\rm ap}^4\right\rangle(\theta)$ to the considered ground truth. The dash-dotted line shows the impact of a finite integration range on $3\left\langle M_{\rm ap}^2\right\rangle^2$, and the other lines on $\left\langle M_{\rm ap}^4\right\rangle$. Gray regions show the 1% and 2% regions.

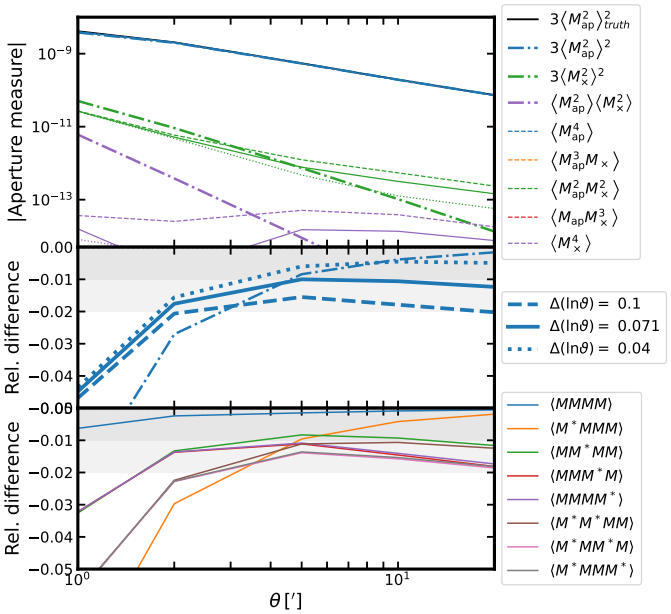

Fig. 5. Effect of the binning accuracy on the fourth-order aperture statistics. (Top-middle) Equivalent to Fig. 4 with radial integration range $[\mathrm{e}^{-2}{}', \mathrm{e}^{5}{}']$ and an increasingly fine hypercubical bin, i.e. $\Delta_\psi = \Delta(\ln\vartheta)$. (Bottom) Relative difference of the eight aperture measures corresponding to the eight natural components to the considered ground truth (see text). Solid lines represent the same set of integration parameters as solid lines in Fig. 4.

which could potentially be computed from a realistic 4PCF. For notational simplicity we defined

$$K_{\mu;ijkmn} = K_\mu\left(\frac{\boldsymbol{q}_{0;ijkmn}}{\theta}, \frac{\boldsymbol{q}_{1;ijkmn}}{\theta}, \frac{\boldsymbol{q}_{2;ijkmn}}{\theta}, \frac{\boldsymbol{q}_{3;ijkmn}}{\theta}\right), \tag{47}$$

with $\boldsymbol{q}_s$ from Eq. (22), $\vartheta_{1;i}$ the arithmetic center of the i-th radial bin, $\psi_{23;m}$ the arithmetic center of the m-th angular bin, and equivalent for the other radial and angular coordinates.

4.3.1. Riemann integrated 4PCF

To emulate the implicit bin-averaging in practical nPCF estimators, we estimate the radially integrated 4PCF by subdividing the original radial bins into r finer bins of width $\delta_{\vartheta;i'}$, such that $\sum_{i'=1}^r \delta_{\vartheta;i'} = \Delta_{\vartheta;i}$. The estimate of the μ-th natural component is

$$\overline{\Gamma_\mu^{\rm Rie}}^\times_{i,j,k,m,n} = \frac{1}{\sum_{i',j',k'=1}^r \delta_{\vartheta;i'}\delta_{\vartheta;j'}\delta_{\vartheta;k'}}$$
$$\times \sum_{i',j',k'=1}^{r} \Gamma_\mu^\times\left(\vartheta_{i'}, \vartheta_{j'}, \vartheta_{k'}, \psi_{12;m}, \psi_{23;n}\right)\delta_{\vartheta;i'}\delta_{\vartheta;j'}\delta_{\vartheta;k'}, \tag{48}$$

with $\vartheta_{i'}$ the arithmetic center of the i'-th fine bin within a coarse bin.

Figure 6 shows $\left\langle M^{(*)4}\right\rangle^p_{\rm Rie,int}(\theta)$ from Eq. (46) with the average shear estimated with Eq. (48). The number of angular bins

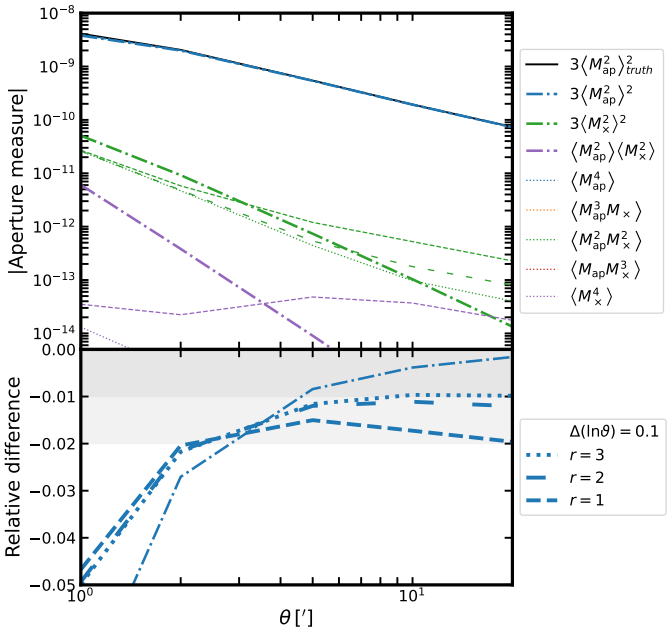

Fig. 6. Increase in the precision on the fourth-order aperture statistics by integrating the 4PCF within a bin with a Riemann sum. Equivalent to Fig. 4 with increasingly fine bins for the 4PCF, $N_{\rm rad,fine} = rN_{\rm rad,coarse}$, and $N_{\rm rad,coarse} = 70$ bins for the filters $[\Delta(\ln\vartheta) = 0.10]$. Dashed lines represent the same set of integration parameters as dashed lines in Fig. 5.

is such that the fine grid has hypercubical bins. In all cases we consider $N_{\rm rad,coarse} = 70$, i.e. $\Delta(\ln\vartheta) = 0.10$, and an increasing r.

Integrating the 4PCF within a coarse bin reduces the finite bin effects on large scales, thus reducing the dispersion between the different aperture measures. Physically, this means that

close-by configurations are now accounted for in the integration scheme also at larger scales. Even with a rather coarse binning of $\Delta(\ln\vartheta) = 0.10$ for the filter we achieve now a high precision on the aperture statistics. This is a favorable result toward the application of the fourth-order shear statistics, because an increase in the number of radial bins for the 4PCFs comes at a larger computational cost.

5. Cosmology with second-, third-, and fourth-order statistics

5.1. Data vector on simulated datasets

We consider as observables the equal-scale aperture statistics

$$\boldsymbol{m} = \left\{\left\langle M_{\rm ap}^2\right\rangle(\theta_\alpha), \left\langle M_{\rm ap}^3\right\rangle(\theta_\beta), \left\langle M_{\rm ap}^4\right\rangle_c(\theta_\gamma)\right\}, \tag{49}$$

with N_θ aperture radii[6]

$$\theta \in \{4.'00, 5.'66, 8.'00, 11.'31, 16.'00\}. \tag{50}$$

We compute the covariance matrix between the observables, C, of dimension $(3N_\theta)^2$, from the full-sky ray-tracing simulations by Takahashi et al. (2017, hereafter T17), assuming a DES-Y3 (Abbott et al. 2022) redshift distribution and shape noise; for more details we refer to the internally estimated covariance from Sect. 6.3.1 in P25.

We extract the cosmological dependence of the observables from the *cosmo*-SLICS simulations by Harnois-Déraps et al. (2019, hereafter cS19). cS19 consists of 26 sets of cosmological parameters,

$$\boldsymbol{\mu} = \{\Omega_{\rm m}, S_8, h, w_0\}, \tag{51}$$

distributed on a latin hypercube. For each cosmology there are 25 light cones, each one with 15–28 noiseless convergence maps of 100 deg^2 at equidistant comoving distance and $z < 3.0$ (Harnois-Déraps et al. 2019). We create DES-Y3-like convergence maps assuming the fiducial DES-Y3 redshift distribution and we estimate the aperture mass moments with the direct estimator from Eq. (15)[7].

We estimate the derivatives of the observables w.r.t. the cosmological parameters with a simulation-based approach. Since the statistics measured on the cS19 are noisy, an estimate through finite differences becomes unstable. We propose a more robust method, where the tangent plane to the observable is constructed by a loss function minimization, which can be easily generalized to high-dimensional parameter space and can account for irregular sampling around the fiducial cosmology, as we find for example with a latin hypercube simulation suite. In Appendix D we describe the method and test for the stability of the derivatives on cS19.

[6] The simulation suite *cosmo*-SLICS (Harnois-Déraps et al. 2019) becomes inaccurate at scales $\theta \lesssim 4'$, where we find the relative error on second-order statistics to be larger than 3% w.r.t. the predictions from the nonlinear cold-dark-matter BACCO emulator (Angulo et al. 2021).

[7] The aperture mass moments are computed with the direct estimator from Eq. (15), using the convolution theorem

$$M_{\rm ap}(\boldsymbol{\vartheta}, \theta) = \mathcal{F}\left[\hat{u}(\theta l)\hat{\kappa}(\boldsymbol{\ell})\right], \tag{52}$$

and Fast Fourier Transforms. In order to avoid finite field effects, we further crop a 4θ boundary on the fields, as suggested by Heydenreich et al. (2023).

5.2. Fisher forecast formalism

The likelihood of the observables given the parameters is

$$\mathcal{L}(\boldsymbol{m}, \boldsymbol{\mu}) = \exp\left\{-\frac{1}{2}\sum_{ij}\left[m_i(\boldsymbol{\mu}) - m_i(\boldsymbol{\mu}_{\rm fid})\right] \times \mathsf{C}_{ij}^{-1}\left[m_j(\boldsymbol{\mu}) - m_j(\boldsymbol{\mu}_{\rm fid})\right]\right\}, \tag{53}$$

where $\boldsymbol{\mu}_{\rm fid}$ are the fiducial values of the parameters (here matched to the cosmological set in cS19 labeled as `fid`, hereafter `cSfid`).

An accurate determination of the parameter posteriors is possible with Bayesian inference, see for example, Burger et al. (2024) for the joint analysis of second- and third-order aperture statistics. However, this requires extensive computational power for the exploration of parameter space and accurate theoretical models for fourth-order shear statistics, both of which are not available.

Assuming a Gaussian likelihood of the observables, the maximum likelihood estimate of the parameters corresponds to the maximum a posteriori from Bayesian inference. The uncertainty on the parameters can then be estimated via the expectation value of the Hessian of the log-likelihood, $\ln\mathcal{L}$, i.e. the Fisher information matrix

$$\mathsf{F}_{qp} = \left\langle\frac{\partial^2(-\ln\mathcal{L})}{\partial\mu_q\partial\mu_p}\right\rangle. \tag{54}$$

If the dependence of the covariance matrix of the observables, C, on the cosmological parameters, $\boldsymbol{\mu}$, can be neglected, then

$$\mathsf{F}_{qp} = \sum_{i,j}\left.\frac{\partial m_i}{\partial\mu_q}\right|_{\mu_{\rm fid}}\mathsf{C}_{ij}^{-1}\left.\frac{\partial m_j}{\partial\mu_p}\right|_{\mu_{\rm fid}} \tag{55}$$

can be estimated through the covariance at the fiducial value (here from T17) and the derivatives at the fiducial value.

Moreover, if the observables are unbiased estimators of their underlying distributions, then $\sqrt{\mathsf{F}_{qq}^{-1}} = \sigma_q$ is the best possible precision on the cosmological parameters with the given observables, according to the Cramér-Rao theorem (Radhakrishna Rao 1945; Cramér 1946), and F^{-1} is the covariance matrix between them.

5.3. Combined forecast second- and higher-order aperture statistics

In Fig. 7 we show the 1σ Fisher ellipse for $\{\Omega_{\rm m}, \sigma_8\}$ for $\left\langle M_{\rm ap}^2\right\rangle$, $\left\langle M_{\rm ap}^3\right\rangle$, and $\left\langle M_{\rm ap}^4\right\rangle$ individually, the joint analysis of second- and third-order statistics, and the joint analysis of second-, third-, and fourth-order statistics, along with the one-dimensional distributions (PDF).

The shaded regions in the PDF represent the 1σ Jackknifing error bars over the cS19 light cones, which affect the width of the Gaussian PDF but not the fiducial `cSfid` value. This error arises from the reduced number of available simulations and does not account for other sources of uncertainty, such as cosmic variance on scales larger than 10° or shape noise. We perform a similar analysis on the two-dimensional distributions in Appendix D.3.

In our setting and within the set of assumptions we cannot report a significant improvement in the constraining power of the aperture statistics when including fourth-order statistics. If there is any information content on the

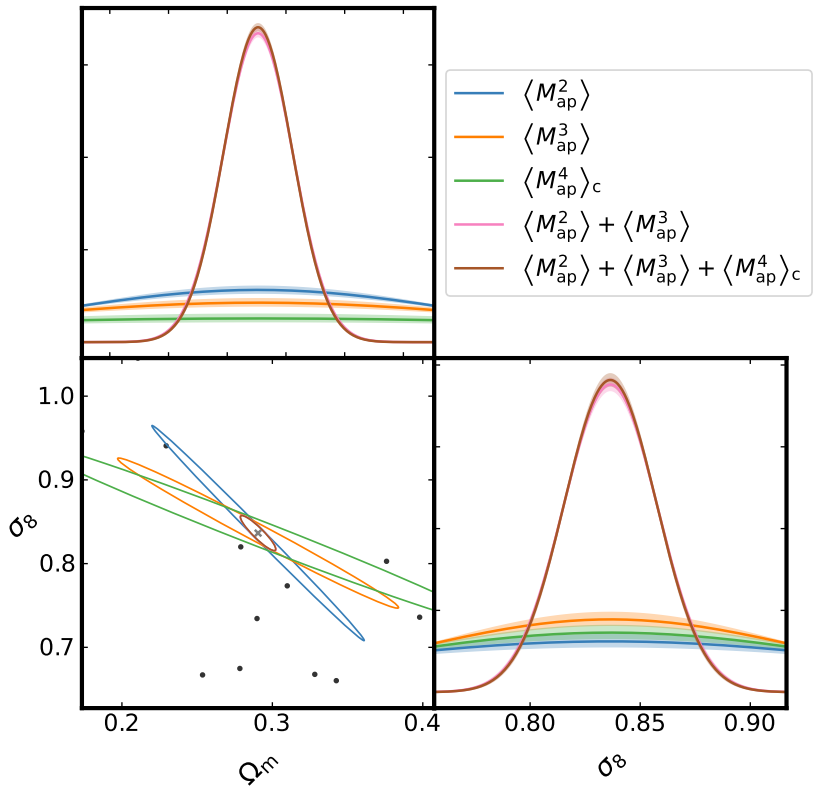

Fig. 7. Joint forecast of second-, third-, and fourth-order aperture statistics, with 1σ contours from the Fisher covariance matrix F^{-1}. The cloud of points in the two-dimensional distribution corresponds to the closest sets of cosmological parameters to the fiducial `cSfid` value, marked with a cross. The Figure of Merit (FoM) of the plotted ellipses, as derived in Appendix D.3, are: FoM($\langle M_{\rm ap}^2 \rangle$) = 104 ± 15, FoM($\langle M_{\rm ap}^3 \rangle$) = 72 ± 20, FoM($\langle M_{\rm ap}^4 \rangle_{\rm c}$) = 29 ± 11, FoM($\langle M_{\rm ap}^2 \rangle + \langle M_{\rm ap}^3 \rangle$) = 652 ± 103, and FoM($\langle M_{\rm ap}^2 \rangle + \langle M_{\rm ap}^3 \rangle + \langle M_{\rm ap}^4 \rangle_{\rm c}$) = 680 ± 106. In the considered setting, the inclusion of fourth-order statistics leads to a nonsignificant improvement in the constraining power of the aperture statistics.

non-tomographic equal-scale fourth-order aperture statistics, we would require the precision of Stage IV surveys, like *Euclid* (Euclid Collaboration: Mellier et al. 2025) and a larger set of simulations or an accurate theoretical model in order to retrieve it.

6. Discussion

The statistical power of Stage IV surveys, like *Euclid* (Euclid Collaboration: Mellier et al. 2025), opens a new range of possibilities for higher-order statistics. Higher moments of the shear field, in the form of shear n-point correlation functions or their projections into the n-th order aperture statistics, are expected to contain part of the non-Gaussian information of the field in their connected part.

Here we explored the relation between n-th order aperture statistics and shear n-point correlation functions (nPCF) or n-point polyspectra. In particular, we derived the explicit expressions for the filters of the fourth-order aperture statistics in terms of the 4PCF and in terms of the trispectrum. On an observed field, the computation through the 4PCF is necessary, as it is not biased by masked regions in the observational field.

We tested the filters for the 4PCF on a model for a shear Gaussian random field (GRF), where the fourth-order statistics only contain disconnected terms, i.e. can be expressed in terms of the second-order statistics. We proposed and tested an integration scheme that provides a two-percent-level precision on the aperture statistics for a GRF, which remains well below the noise budget for Stage IV surveys.

We find deviations from the expected values on very small and very large scales due to an E- and B-mode mixing, similar to the one described in Kilbinger et al. (2006) for second-order aperture statistics. This mode-mixing enters fourth-order statistics through an incomplete radial integration range (see Fig. 4) and an insufficient binning accuracy (see Fig. 5). Despite the stronger impact of these effects on some of the complex aperture measures (see Fig. 3), a separation into modes is only possible when all the complex aperture measures are considered. We achieve the desired precision for an observational range of $\theta \in [2', 20']$, a radial integration range of $\vartheta \in [e^{-2}', e^{5}']$, and a logarithmic binning accuracy of $\Delta(\ln \vartheta) = 0.07$ with hypercubical bins.

The E- and B-mode mixing should be taken into account when obtaining the connected fourth-order statistics for a general field, as the predictions from second-order statistics only correspond to the disconnected terms of $\langle M_{\rm ap}^4 \rangle$ up to a degree determined by the integration range and binning accuracy.

Moreover, we find that using a more realistic model for the 4PCF, where the shear is integrated over radial bins, reduces the required binning accuracy on the 4PCF to $\Delta(\ln \vartheta) = 0.10$, which is broad enough to be estimated on Stage III data. P25 develop a multipole-based 4PCF estimator and use the integration method described here to obtain a significant detection of fourth-order aperture statistics. They also find that the error estimations presented here for a GRF closely match the observed errors in the $\langle M_{\rm ap}^4 \rangle_{\rm c}$-statistics measured on DES-Y3 (Abbott et al. 2022).

Finally, we computed a Fisher forecast for joint second-, third-, and fourth-order aperture statistics on a DES-Y3-like setup. To do so, we suggest a robust method for estimating derivatives from simulations, which we tested on the *cosmo*-SLICS (Harnois-Déraps et al. 2019) simulation suite.

We do not find a significant improvement in the constraining power of the aperture statistics when including fourth-order statistics in a $\langle M_{\rm ap}^2 \rangle + \langle M_{\rm ap}^3 \rangle$ joint analysis, which we believe is driven by the given set of assumptions. These assumptions are:

– Due to the nature of Fisher forecasts, we assume a Gaussian distribution of the observables, which is not a good approximation for $\langle M_{\rm ap}^3 \rangle$ (Euclid Collaboration: Ajani et al.

2023) nor $\langle M_{\rm ap}^4 \rangle_{\rm c}$ (P25). The Fisher ellipses are thus not able to fully capture the degeneracies of the observables.
- From a theoretical point of view, we assumed that equal-scale aperture statistics contain most of the information to the given order, if a sufficiently large part of the field is available. This is exact for $\langle M_{\rm ap}^2 \rangle$ and a good approximation for $\langle M_{\rm ap}^3 \rangle$ if one considers tomography (see e.g., Burger et al. 2024). Equal-scale aperture moments contain, for increasing order, a smaller fraction of the total information in the given order. Due to the strong correlation between neighboring scales and neighboring orders seen in the covariance matrix from T17 (see Fig. 4 in P25), we expect that a few combinations of unequal scales contain most of the information on the multi-scale aperture moments, and leave this analysis to future work.
- From the parameters considered in cS19, we marginalized over the dependence on h and w_0. This reduces the relative constraining power of higher-order aperture statistics with respect to second-order ones, if their dependence on such parameters is stronger than for second-order statistics.
  We recovered a low constraining power on the evolution parameters, such as w_0, due to lack of tomography. When studying the derivatives from the samples in Appendix D.2, we find a small scatter in the derivatives with respect to $\Omega_{\rm m}$ that is reduced if we also consider the parameter w_0, i.e. the scatter on $\Omega_{\rm m}$ is influenced by the given dark energy model. Considering tomography would weaken this degeneracy due to the different evolution of the different energy components.
- Higher-order aperture mass moments have an increasingly stronger decay with aperture radius, so most of the information in fourth-order statistics is at small scales (assuming no shape noise), which are not available in the simulations used for the derivatives, and are even more challenging to model.
- Furthermore, we studied the effect of using the derivatives from theory on the Fisher ellipses for second-order, third-order, and the joint second- and third-order statistics. We find that the relative constraining power of a joint analysis $\langle M_{\rm ap}^2 \rangle + \langle M_{\rm ap}^3 \rangle$ is overestimated when computing derivatives from cS19. This unrealistic degeneracy breaking for a joint second- and third-order analysis can result in a lower relative constraining power of fourth-order statistics[8].

In our analysis we do not consider any nuisance parameters. Even if fourth-order statistics were fully degenerate with the lower-order moments (after relaxing all mentioned assumptions), they would have a different degeneracy direction for the nuisance parameters. Pyne & Joachimi (2021) suggest the use of third-order statistics to calibrate second-order statistics. On Stage IV surveys, where both second- and third-order moments are used to constrain cosmology, fourth-order statistics could become a consistency check and a test for systematics.

We therefore conclude that performing a full cosmological analysis for fourth-order aperture statistics on a Stage III survey, such as DES-Y3 (Abbott et al. 2022), would on to a minimal improvement on the cosmological constraints.

We developed and thoroughly tested a method targeted to Stage IV surveys, such as *Euclid* (Euclid Collaboration: Mellier et al. 2025), where the unprecedented precision will increase the significance of higher-order statistics and enable, for example, a tomographic analysis of $\langle M_{\rm ap}^4 \rangle_{\rm c}$. Under that setting, it will be possible to determine whether fourth-order shear statistics break degeneracies between second- and third-order statistics, or if they are degenerate with the previous orders, in which case they can be used to help in the determination of the nuisance parameters.

Acknowledgements. We would like to thank Joachim Harnois-Déraps for providing us access to the *cosmo*-SLICS mock data. LP acknowledges support from the DLR grant 50QE2302. LL is supported by the Austrian Science Fund (FWF) [ESP 357-N].

References

Abbott, T. M. C., Aguena, M., Alarcon, A., et al. 2022, Phys. Rev. D, 105, 023520
Amon, A., Gruen, D., Troxel, M. A., et al. 2022, Phys. Rev. D, 105, 023514
Angulo, R. E., Zennaro, M., Contreras, S., et al. 2021, MNRAS, 507, 5869
Bartelmann, M., & Schneider, P. 2001, Phys. Rep., 340, 291
Bernardeau, F., Colombi, S., Gaztañaga, E., & Scoccimarro, R. 2002, Phys. Rep., 367, 1
Burger, P. A., Porth, L., Heydenreich, S., et al. 2024, A&A, 683, A103
Chisari, N. E., Alonso, D., Krause, E., et al. 2019, ApJS, 242, 2
Cramér, H. 1946, Mathematical Methods of Statistics (Princeton: Princeton University Press)
Crittenden, R. G., Natarajan, P., Pen, U.-L., & Theuns, T. 2002, ApJ, 568, 20
Dalal, R., Li, X., Nicola, A., et al. 2023, Phys. Rev. D, 108, 123519
Euclid Collaboration (Blanchard, A., et al.) 2020, A&A, 642, A191
Euclid Collaboration (Ajani, V., et al.) 2023, A&A, 675, A120
Euclid Collaboration (Mellier, Y., et al.) 2025, A&A, 697, A1
Friedmann, A. 1922, Z. Phys., 10, 377
Harnois-Déraps, J., Giblin, B., & Joachimi, B. 2019, A&A, 631, A160
Heydenreich, S., Linke, L., Burger, P., & Schneider, P. 2023, A&A, 672, A44
Hunter, J. D. 2007, Comput. Sci. Eng., 9, 90
Isserlis, L. 1918, Biometrika, 12, 134
Jarvis, M., Bernstein, G., & Jain, B. 2004, MNRAS, 352, 338
Kaiser, N., & Squires, G. 1993, ApJ, 404, 441
Kilbinger, M. 2015, Rep. Progr. Phys., 78, 086901
Kilbinger, M., Schneider, P., & Eifler, T. 2006, A&A, 457, 15
Kuijken, K., Heymans, C., Hildebrandt, H., et al. 2015, MNRAS, 454, 3500
Li, X., Zhang, T., Sugiyama, S., et al. 2023, Phys. Rev. D, 108, 123518
Limber, D. N. 1953, ApJ, 117, 134
Mandelbaum, R. 2018, ARA&A, 56, 393
Munshi, D., & Coles, P. 2003, MNRAS, 338, 846
Porth, L., & Smith, R. E. 2021, MNRAS, 508, 3474
Porth, L., Smith, R. E., Simon, P., Marian, L., & Hilbert, S. 2020, MNRAS, 499, 2474
Porth, L., Heydenreich, S., Burger, P., Linke, L., & Schneider, P. 2024, A&A, 689, A227
Porth, L., Silvestre-Rosello, E., Schneider, P., & Larma, M. 2025, arXiv e-prints, (Paper II) [arXiv:2509.07974]
Pyne, S., & Joachimi, B. 2021, MNRAS, 503, 2300
Radhakrishna Rao, C. 1945, Bull. Calcutta Math. Soc., 37, 81
Schneider, P. 1996, MNRAS, 283, 837
Schneider, P. 2003, A&A, 408, 829
Schneider, P., & Lombardi, M. 2003, A&A, 397, 809
Schneider, P., van Waerbeke, L., Jain, B., & Kruse, G. 1998, MNRAS, 296, 873
Schneider, P., van Waerbeke, L., & Mellier, Y. 2002, A&A, 389, 729
Schneider, P., Kilbinger, M., & Lombardi, M. 2005, A&A, 431, 9
Secco, L. F., Samuroff, S., Krause, E., et al. 2022, Phys. Rev. D, 105, 023515
Stölzner, B., Wright, A. H., Asgari, M., et al. 2025, A&A, 702, A169
Takahashi, R., Hamana, T., Shirasaki, M., et al. 2017, ApJ, 850, 24
Takahashi, R., Nishimichi, T., Namikawa, T., et al. 2021, Astrophysics Source Code Library [record ascl:2106.031]
Wright, A. H., Stölzner, B., Asgari, M., et al. 2025, A&A, 703, A158
Yahia-Cherif, S., Blanchard, A., Camera, S., et al. 2021, A&A, 649, A52

[8] We compute the relative constraining power as the ratio of the correspondent Figures of Merit, see Eq. (D.10).

Appendix A: Conversion from *n*PCF to aperture statistics

A.1. Derivation of filters

In order to obtain a E/B-decomposed aperture statistics it is necessary to convert the 2^{n-1} natural components of the shear nPCF to their corresponding complex aperture measures. We only present a detailed derivation for the special case of all aperture radii being equal, $\theta_1 = \theta_2 = \cdots, \theta_{n-1} \equiv \theta$ and later mention the modifications to the expressions when allowing for arbitrary configurations of aperture radii.

As the derivations for all filter functions, $F_\mu^{(n)}$, are structurally equivalent, we only explicitly derive the filter $\langle (M^*)^p M^{n-p}\rangle$, corresponding to the μ_p-th natural component of the nPCF. We begin by reordering the expression for the $\langle (M^*)^p M^{n-p}\rangle$ correlator:

$$
\begin{aligned}
&\langle (M^*)^p M^{n-p}\rangle(\theta) \\
&\quad\equiv \int \mathrm{d}^2\mathbf{X}_0 \int \mathrm{d}^2\boldsymbol{\vartheta}_1 \cdots \int \mathrm{d}^2\boldsymbol{\vartheta}_{n-1}\; Q_\theta(|\mathbf{X}_0|)\cdots Q_\theta(|\mathbf{X}_0+\boldsymbol{\vartheta}_{n-1}|) \\
&\qquad\times \left\langle \gamma^*_{\mathrm{cart}}(\mathbf{X}_0)\cdots\gamma^*_{\mathrm{cart}}(\mathbf{X}_0+\boldsymbol{\vartheta}_{p-1})\gamma_{\mathrm{cart}}(\mathbf{X}_0+\boldsymbol{\vartheta}_p)\cdots\gamma_{\mathrm{cart}}(\mathbf{X}_0+\boldsymbol{\vartheta}_{n-1})\right\rangle \; \mathrm{e}^{-2\mathrm{i}\left(-\zeta_0-\cdots-\zeta_{p-1}+\zeta_p+\cdots+\zeta_{n-1}\right)} \\
&\quad= \int \mathrm{d}^2\boldsymbol{\vartheta}_1\cdots\int \mathrm{d}^2\boldsymbol{\vartheta}_{n-1}\,\Gamma^{\mathrm{cart}}_{\mu_p}(\boldsymbol{\vartheta}_1,\cdots,\boldsymbol{\vartheta}_{n-1}) \int \mathrm{d}^2\mathbf{X}_0\, \frac{\left(\breve{\mathbf{X}}_0\right)^2}{\left|\breve{\mathbf{X}}_0\right|^2}\cdots\frac{\left(\breve{\mathbf{X}}_0+\breve{\boldsymbol{\vartheta}}_{p-1}\right)^2}{\left|\breve{\mathbf{X}}_0+\breve{\boldsymbol{\vartheta}}_{p-1}\right|^2}\frac{\left(\breve{\mathbf{X}}^*_0+\breve{\boldsymbol{\vartheta}}^*_{p}\right)^2}{\left|\breve{\mathbf{X}}_0+\breve{\boldsymbol{\vartheta}}_{p}\right|^2}\cdots\frac{\left(\breve{\mathbf{X}}^*_0+\breve{\boldsymbol{\vartheta}}^*_{n-1}\right)^2}{\left|\breve{\mathbf{X}}_0+\breve{\boldsymbol{\vartheta}}_{n-1}\right|^2} \\
&\qquad\times \frac{\left|\breve{\mathbf{X}}_0\right|^2\cdots\left|\breve{\mathbf{X}}_0+\breve{\boldsymbol{\vartheta}}_{n-1}\right|^2}{(4\pi\theta^4)^n}\;\exp-\frac{1}{2\theta^2}\left(\left|\breve{\mathbf{X}}_0\right|^2+\sum_{\ell=1}^{n-1}\left|\breve{\mathbf{X}}_0+\breve{\boldsymbol{\vartheta}}_\ell\right|^2\right) \\
&\quad= \int \mathrm{d}^2\boldsymbol{\vartheta}_1\cdots\int \mathrm{d}^2\boldsymbol{\vartheta}_{n-1}\,\Gamma^{\mathrm{cart}}_{\mu_p}(\boldsymbol{\vartheta}_1,\cdots,\boldsymbol{\vartheta}_{n-1})\;\exp-\frac{1}{2\theta^2}\sum_{\ell=0}^{n-1}\left|\boldsymbol{q}_\ell\right|^2 \\
&\qquad\times \int \mathrm{d}^2\mathbf{X}_0\,\frac{\left(\breve{\mathbf{X}}_0\right)^2\cdots\left(\breve{\mathbf{X}}_0+\breve{\boldsymbol{\vartheta}}_{p-1}\right)^2\left(\breve{\mathbf{X}}^*_0+\breve{\boldsymbol{\vartheta}}^*_{p}\right)^2\cdots\left(\breve{\mathbf{X}}^*_0+\breve{\boldsymbol{\vartheta}}^*_{n-1}\right)^2}{(4\pi\theta^4)^n}\;\exp-\frac{n}{2\theta^2}\left|\mathbf{X}_0-\boldsymbol{q}_0\right|^2\;,
\end{aligned}
\tag{A.1}
$$

where in the second step we used the expression (14) of the Q-filter and in the third step rewrote the exponential using the n vectors $\{\boldsymbol{q}_\mu\}$ connecting the centroid of the points $\{\mathbf{X}_\mu\}$ with $\mathbf{X}_\mu$; $\boldsymbol{q}_0 = -\frac{1}{n}\sum_{i=1}^{n-1}\boldsymbol{\vartheta}_i$ and $\boldsymbol{q}_i = \boldsymbol{q}_0+\boldsymbol{\vartheta}_i$; and further used the property $\sum_{\mu=0}^{n-1}\boldsymbol{q}_\mu = 0$.

Now focusing our attention to the innermost integral, I, we can make the substitution $\mathbf{Z} = \mathbf{X}_0 - \boldsymbol{q}_0$ and rewrite I in polar coordinates:

$$
I \sim \int \mathrm{d}Z\, Z\, \mathrm{e}^{-\frac{n}{2\theta^2}Z^2}\int_0^{2\pi}\mathrm{d}\varphi_Z\left[\prod_{\ell=0}^{p-1}\left(\breve{Z}+\breve{\boldsymbol{q}}_\ell\right)^2\right]\left[\prod_{\ell=p}^{n-1}\left(\breve{Z}^*+\breve{\boldsymbol{q}}^*_\ell\right)^2\right]. \tag{A.2}
$$

In this form we note that when expanding the products, the only terms that give a nonvanishing contribution to I are of the form $c(\breve{\boldsymbol{q}}_0,\cdots,\breve{\boldsymbol{q}}_{n-1})\;|\mathbf{Z}|^{2k}$. For being able to write down the corresponding prefactors, we make use of Vietas formulas, which give the coefficients when expanding out a factorized polynomial of order n,

$$
\prod_{i=1}^{n}(x+x_i) = \sum_{k=0}^{n} e_k(x_1,\cdots,x_n)\,x^{n-k} \qquad ; \qquad e_k(x_1,\cdots,x_n) = \sum_{1\le i_1<\cdots<i_k\le n} x_{i_1}\cdots x_{i_n} \text{ and } e_0(x_1,\cdots,x_n) = 1\;, \tag{A.3}
$$

where $e_k(x_1,\cdots,x_n)$ denotes the elementary symmetric polynomial of degree k in n variables. We can apply these relations to both products in (A.2), evaluate the integral over ψ_1 order-by-order and solve the remaining Gaussian integral, yielding:

$$
I \sim (2\pi)\sum_{k=0}^{2p}\frac{k!\,2^k\,\theta^{2(k+1)}}{n^{k+1}}\,e_{2p-k}(\breve{\boldsymbol{q}}_0,\breve{\boldsymbol{q}}_0,\breve{\boldsymbol{q}}_1,\breve{\boldsymbol{q}}_1,\cdots,\breve{\boldsymbol{q}}_{p-1},\breve{\boldsymbol{q}}_{p-1})e_{2(n-p)-k}(\breve{\boldsymbol{q}}^*_p,\breve{\boldsymbol{q}}^*_p,\breve{\boldsymbol{q}}^*_{p+1},\breve{\boldsymbol{q}}^*_{p+1},\cdots,\breve{\boldsymbol{q}}^*_{n-1},\breve{\boldsymbol{q}}^*_{n-1})\,. \tag{A.4}
$$

We note that the e_k themselves can readily be allocated recursively via the Newton identities. Finally, plugging (A.4) into (A.1), substituting the relation between the $\times$-projection and the Cartesian projection of Γ_{μ_p} and rearranging a bit we have

$$
\begin{aligned}
\langle (M^*)^p M^{n-p}\rangle(\theta) = &\int\frac{\mathrm{d}\vartheta_1\,\vartheta_1}{\theta^2}\cdots\int\frac{\mathrm{d}\vartheta_{n-1}\,\vartheta_{n-1}}{\theta^2}\int\frac{\mathrm{d}\phi_{1\,2}}{2\pi}\cdots\int\frac{\mathrm{d}\phi_{1\,n-1}}{2\pi} \\
&\times\Gamma^{\times}_{\mu_p}(\boldsymbol{\vartheta}_1,\cdots,\boldsymbol{\vartheta}_{n-1})\,\mathrm{e}^{2\mathrm{i}\left[\sum_{\ell=2}^{n-2}\beta^{\mu_p}_{\ell+1}\phi_{1\,\ell}+\left(0.5\beta^{\mu_p}_1+\beta^{\mu_p}_n\right)\phi_{1\,n-1}\right]}\,F^{(n)}_{\mu_p}\left(\frac{\breve{\boldsymbol{q}}_0}{\theta},\cdots\frac{\breve{\boldsymbol{q}}_{n-1}}{\theta}\right),
\end{aligned}
\tag{A.5}
$$

$$
F^{(n)}_{\mu_p}(\breve{\boldsymbol{q}}_0,\cdots\breve{\boldsymbol{q}}_{n-1}) = \mathrm{e}^{-\frac{1}{2}\left(\sum_{\mu=0}^{n-1}|\breve{\boldsymbol{q}}_\mu|^2\right)}\sum_{k=0}^{2p}\frac{k!\;e_{2p-k}(\breve{\boldsymbol{q}}_0,\breve{\boldsymbol{q}}_0,\breve{\boldsymbol{q}}_1,\breve{\boldsymbol{q}}_1,\cdots,\breve{\boldsymbol{q}}_{p-1},\breve{\boldsymbol{q}}_{p-1})\,e_{2(n-p)-k}(\breve{\boldsymbol{q}}^*_p,\breve{\boldsymbol{q}}^*_p,\breve{\boldsymbol{q}}^*_{p+1},\breve{\boldsymbol{q}}^*_{p+1},\cdots,\breve{\boldsymbol{q}}^*_{n-1},\breve{\boldsymbol{q}}^*_{n-1})}{2^{n-k}\,n^{k+1}}\,, \tag{A.6}
$$

where we performed the integral over φ_1 owing to statistical isotropy and set $\varphi_1 \equiv 0$ in all relations depending on φ_1.

A.2. Modifications for unequal aperture radii

Much of the above derivation can be reused when allowing for different filter radii θ_μ. First, in resemblance to (A.1), we have

$$\begin{aligned}\langle (M^*)^p M^{n-p}\rangle(\theta_0,\cdots,\theta_{n-1}) = &\int \mathrm{d}^2\boldsymbol{\vartheta}_1\cdots\int \mathrm{d}^2\boldsymbol{\vartheta}_{n-1}\,\Gamma^{\mathrm{cart}}_{\mu_p}(\boldsymbol{\vartheta}_1,\cdots,\boldsymbol{\vartheta}_{n-1})\;\mathrm{e}^{-c/2}\\ \times\int \mathrm{d}^2\mathbf{X}_0\,&\frac{\left(\breve{\mathbf{X}}_0\right)^2\cdots\left(\breve{\mathbf{X}}_0+\breve{\boldsymbol{\vartheta}}_{p-1}\right)^2\left(\breve{\mathbf{X}}_0^*+\breve{\boldsymbol{\vartheta}}_p^*\right)^2\cdots\left(\breve{\mathbf{X}}_0^*+\breve{\boldsymbol{\vartheta}}_{n-1}^*\right)^2}{(4\pi)^n(\theta_0\cdots\theta_{n-1})^4}\;\mathrm{e}^{-(\mathbf{X}_0-\mathbf{b})^2/(2a^2)}\;,\\ &\text{where}\;\; a^{-2}\equiv\sum_{i=0}^{n-1}\theta_i^{-2}\;,\qquad \mathbf{b}\equiv -a^2\sum_{i=0}^{n-1}\frac{\boldsymbol{\vartheta}_i}{\theta_i^2}\;,\qquad c\equiv\left(\sum_{i=0}^{n-1}\frac{|\vartheta_i|^2}{\theta_i^2}\right)-\frac{|\mathbf{b}|^2}{a^2}\;.\end{aligned}\tag{A.7}$$

The integral I is defined and evaluated using the same procedure as in the steps leading to (A.4) and we find

$$I\sim(2\pi)\sum_{k=0}^{2p}k!\,2^k\,a^{2(k+1)}\;e_{2p-k}(\breve{\mathbf{d}}_0,\breve{\mathbf{d}}_0,\breve{\mathbf{d}}_1,\breve{\mathbf{d}}_1,\cdots,\breve{\mathbf{d}}_{p-1},\breve{\mathbf{d}}_{p-1})\,e_{2(n-p)-k}(\breve{\mathbf{d}}_p^*,\breve{\mathbf{d}}_p^*,\breve{\mathbf{d}}_{p+1}^*,\breve{\mathbf{d}}_{p+1}^*,\cdots,\breve{\mathbf{d}}_{n-1}^*,\breve{\mathbf{d}}_{n-1}^*)\,,\tag{A.8}$$

where we defined $\breve{\mathbf{d}}_k\equiv\breve{\mathbf{b}}+\breve{\boldsymbol{\vartheta}}_k$ and we set $\breve{\boldsymbol{\vartheta}}_0\equiv 0$.

A.3. Separation in E- and B-modes

The 2^{n-1} complex aperture measures corresponding to the integral over the natural components contain both E- and B-mode contributions. The general mode-separating aperture statistic of n-th order is

$$\left\langle M_{\mathrm{ap}}^{n-q}M_\times^q\right\rangle(\theta)=\langle\Re M^{n-q}\Im M^q\rangle(\theta)=\left\langle\left(|M|\Re\mathrm{e}^{\mathrm{i}\phi}\right)^{n-q}\left(|M|\Im\mathrm{e}^{\mathrm{i}\phi}\right)^q\right\rangle(\theta)=\left\langle|M|^n\Re\mathrm{e}^{\mathrm{i}\phi n-q}\Im\mathrm{e}^{\mathrm{i}\phi q}\right\rangle(\theta),\tag{A.9}$$

where $q\in\{0,...,n\}$ is the number of cross apertures and we used the polar notation for the complex aperture $M=|M|\mathrm{e}^{\mathrm{i}\phi}$ and the definition of the aperture mass Eq. (10). In a similar way, the complex aperture measures

$$\langle(M^*)^pM^{n-p}\rangle(\theta)=\left\langle(|M|\mathrm{e}^{-\mathrm{i}\phi})^p(|M|\mathrm{e}^{\mathrm{i}\phi})^{n-p}\right\rangle(\theta)=\left\langle|M|^n\mathrm{e}^{(n-2p)\mathrm{i}\phi}\right\rangle(\theta).\tag{A.10}$$

The integrals over the different natural components with p conjugated shears contain different information about the field and should all be computed in order to extract the maximum information about the field, in the presence of tomography and shape noise. We define A_{np} as the average of the $\binom{n}{p}$ complex aperture measures with p complex apertures, which formally follow the same expression as Eq. (A.10).

We can express the aperture statistics as a linear combination over the different complex aperture measures with real coefficients C_{qp}

$$\left\langle M_{\mathrm{ap}}^{n-q}M_\times^q\right\rangle(\theta)=\sum_{p=0}^{\lfloor n/2\rfloor}C_{qp}\times\left(\Re A_{np}\text{ or }\Im A_{np}\right),\tag{A.11}$$

where we find the real value for q even, and the imaginary one for q odd.

Using the properties of the complex numbers, $\Re z=(z+z^*)/2$ and $\Im z=(z-z^*)/(2\,\mathrm{i})$, and the commutativity of the ensemble averages with additions, we obtain the coefficients C_{qp} through

$$\frac{1}{2^n\,\mathrm{i}^q}\left(\mathrm{e}^{\mathrm{i}\phi}+\mathrm{e}^{-\mathrm{i}\phi}\right)^{n-q}\left(\mathrm{e}^{\mathrm{i}\phi}-\mathrm{e}^{-\mathrm{i}\phi}\right)^q=\frac{1}{2\,\mathrm{i}^{q_{\mathrm{mod}2}}}\sum_{p=0}^{\lfloor n/2\rfloor}C_{qp}\times\left(\mathrm{e}^{(n-2p)\mathrm{i}\phi}+(-1)^q\mathrm{e}^{-(n-2p)\mathrm{i}\phi}\right).\tag{A.12}$$

The different coefficients can be obtained by comparison of both sides on Eq. (A.12); see Table A.1 for the values for $n=3,4,5$. The coefficients for the pure E-mode, $q=0$, further simplify to

$$C_{0p}=\frac{1}{2^{n-1}}\binom{p}{n}\left[1-\frac{\delta^{\mathrm{K}}_{p-n/2}}{2}\right].\tag{A.13}$$

Table A.1. Coefficients for the linear combinations of complex aperture measures to give an E- and B-mode separation, as in Eq. (A.11). Computed from Eq. (A.12). The coefficients are only defined for $q \leq n$, being the ones for $n = 3$ and $n = 4$ compatible with the ones presented by Jarvis et al. (2004). The values marked with × are undefined by Eq. (A.12), so we can set them to 0, as in Sect. 3.2.2.

n	C_{0p}	C_{1p}	C_{2p}	C_{3p}	C_{4p}	C_{5p}
3	$\{1/4, 3/4\}$	$\{1/4, 1/4\}$	$\{-1/4, 1/4\}$	$\{-1/4, 3/4\}$	–	–
4	$\{1/8, 1/2, 3/8\}$	$\{1/8, 1/4, \times\}$	$\{-1/8, 0, 1/8\}$	$\{-1/8, 1/4, \times\}$	$\{1/8, -1/2, 3/8\}$	–
5	$\{1/16, 5/16, 5/8\}$	$\{1/16, 3/16, 1/8\}$	$\{-1/16, -1/16, 1/8\}$	$\{-1/16, 1/16, 1/8\}$	$\{1/16, -3/16, 1/8\}$	$\{1/16, -5/16, 5/8\}$

Appendix B: Conversion from 4PCF to aperture statistics

B.1. Derivation of filters

The aperture for the 4th order without conjugated shear is

$$\begin{aligned}\langle M^4\rangle(\theta) &= \int \mathrm{d}^2X_0 \cdots \int \mathrm{d}^2X_3 \left(\prod_{i=0}^{3} Q_\theta(|\boldsymbol{X}_i|)\frac{\breve{X}_i^{*^2}}{|\breve{X}_i|^2}\right)\Gamma_0^{\mathrm{cart}}(\boldsymbol{X}_1-\boldsymbol{X}_0, \boldsymbol{X}_2-\boldsymbol{X}_0, \boldsymbol{X}_3-\boldsymbol{X}_0)\\ &= \int \mathrm{d}^2\vartheta_1 \cdots \int \mathrm{d}^2\vartheta_3 \int \mathrm{d}^2X_0\, \Gamma_0^{\mathrm{cart}}(\boldsymbol{\vartheta}_1, \boldsymbol{\vartheta}_2, \boldsymbol{\vartheta}_3)\frac{1}{(4\pi\theta^4)^4}\left[\prod_{i=1}^{3}\left(\breve{X}_0^* + \breve{\vartheta}_i^*\right)^2\right]\breve{X}_0^{*2}\exp -\frac{|\boldsymbol{X}_0|^2 + \sum_{i=1}^{3}|\boldsymbol{X}_0+\boldsymbol{\vartheta}_i|^2}{2\theta^2},\end{aligned} \tag{B.1}$$

where we chose the Cartesian projection for the shear and in the last step we changed to a reference system centered in $\boldsymbol{X}_0$ and used the filter by Crittenden et al. (2002) from Eq. (14). The polynomial in the exponent can be rewritten as $4(\boldsymbol{X}_0 - \boldsymbol{q}_0)^2 + \sum_{i=0}^{3}(|\boldsymbol{q}_i|^2)$, so if we change the integration over $\boldsymbol{X}_0$ to the center of mass of the quadrilateral, where $\boldsymbol{X}_0 = \boldsymbol{Z} + \boldsymbol{q}_0$, in polar coordinates

$$\langle M^4\rangle(\theta) = \frac{1}{(4\pi\theta^4)^4}\int \mathrm{d}^2\vartheta_1 \cdots \int \mathrm{d}^2\vartheta_3\, \Gamma_0^{\mathrm{cart}}(\boldsymbol{\vartheta}_1, \boldsymbol{\vartheta}_2, \boldsymbol{\vartheta}_3)\int \mathrm{d}Z\, Z\exp -\frac{4Z^2 + \sum_{i=0}^{3}|\boldsymbol{q}_i|^2}{2\theta^2}\int \mathrm{d}\varphi_Z \prod_{i=0}^{3}\left[\left(\breve{Z}^* + \breve{q}_i^*\right)^2\right].$$

Both the integrals over φ_Z and Z can be carried out analytically, giving

$$\begin{aligned}\langle M^4\rangle(\theta) &= \frac{1}{(4\pi\theta^4)^4}\int \mathrm{d}^2\vartheta_1 \cdots \int \mathrm{d}^2\vartheta_3\, \Gamma_0^{\mathrm{cart}}(\boldsymbol{\vartheta}_1, \boldsymbol{\vartheta}_2, \boldsymbol{\vartheta}_3)\left(\prod_{i=0}^{3}\breve{q}_i^{*2}\exp -\frac{|\boldsymbol{q}_i|^2}{2\theta^2}\right)\frac{2\pi\theta^2}{4}\\ &= \int \frac{\mathrm{d}\vartheta_1\,\vartheta_1}{\theta^2}\cdots\int\frac{\mathrm{d}\vartheta_3\,\vartheta_3}{\theta^2}\int\frac{\mathrm{d}\psi_{12}}{2\pi}\int\frac{\mathrm{d}\psi_{23}}{2\pi}K_0\left(\frac{\boldsymbol{q}_0}{\theta},\frac{\boldsymbol{q}_1}{\theta},\frac{\boldsymbol{q}_2}{\theta},\frac{\boldsymbol{q}_3}{\theta}\right)P_0^{\mathrm{cart},\times}(\boldsymbol{\vartheta}_1,\boldsymbol{\vartheta}_2,\boldsymbol{\vartheta}_3)\,\Gamma_0^{\times}(\vartheta_1,\vartheta_2,\vartheta_3,\psi_{12},\psi_{23}),\end{aligned} \tag{B.2}$$

where we defined the filter function K_0 from Eq. (28) by integrating over φ_1, since both the shear 4PCF and the combination of filter and projector are equivalent under a total rotation of a quadrilateral. Following the definition from Sect. 3.1, $P_\mu^{\mathrm{cart},\times}(\boldsymbol{\vartheta}_1,\boldsymbol{\vartheta}_2,\boldsymbol{\vartheta}_3) = \left[P_\mu^{\times,\mathrm{cart}}(\boldsymbol{\vartheta}_1,\boldsymbol{\vartheta}_2,\boldsymbol{\vartheta}_3)\right]^*$.

When one of the vertices of the quadrilateral has a conjugated shear

$$\begin{aligned}\langle M^* M^3\rangle(\theta) &= \int \mathrm{d}^2X_0 \cdots \int \mathrm{d}^2X_3 \prod_{i=0}^{3}\left[Q_\theta(|\boldsymbol{X}_i|)\right]\prod_{j=1}^{3}\left(\frac{\breve{X}_j^{*2}}{|\breve{X}_j|^2}\right)\frac{\breve{X}_0^{\,2}}{|\breve{X}_0|^2}\,\Gamma_1^{\mathrm{cart}}(\boldsymbol{X}_1-\boldsymbol{X}_0,\boldsymbol{X}_2-\boldsymbol{X}_0,\boldsymbol{X}_3-\boldsymbol{X}_0)\\ &= \frac{1}{(4\pi\theta^4)^4}\int \mathrm{d}^2\vartheta_1 \cdots \int \mathrm{d}^2\vartheta_3\,\Gamma_1^{\mathrm{cart}}(\boldsymbol{\vartheta}_1,\boldsymbol{\vartheta}_2,\boldsymbol{\vartheta}_3)\int \mathrm{d}Z\,Z\exp -\frac{4Z^2+\sum_{i=0}^{3}|\boldsymbol{q}_i|^2}{2\theta^2}\int \mathrm{d}\varphi_Z\prod_{j=1}^{3}\left[(\breve{Z}^*+\breve{q}_j^*)^2\right](\breve{Z}+\breve{q}_0)^2\\ &= \int \frac{\mathrm{d}\vartheta_1\,\vartheta_1}{\theta^2}\cdots\int\frac{\mathrm{d}\vartheta_3\,\vartheta_3}{\theta^2}\int\frac{\mathrm{d}\psi_{12}}{2\pi}\int\frac{\mathrm{d}\psi_{23}}{2\pi}K_1\left(\frac{\boldsymbol{q}_0}{\theta},\frac{\boldsymbol{q}_1}{\theta},\frac{\boldsymbol{q}_2}{\theta},\frac{\boldsymbol{q}_3}{\theta}\right)P_1^{\mathrm{cart},\times}(\boldsymbol{\vartheta}_1,\boldsymbol{\vartheta}_2,\boldsymbol{\vartheta}_3)\,\Gamma_1^{\times}(\vartheta_1,\vartheta_2,\vartheta_3,\psi_{12},\psi_{23}),\end{aligned} \tag{B.3}$$

where we proceeded as for $\langle M^4\rangle(\theta)$.

When two of the vertices have conjugated shear

$$\begin{aligned}\langle M^{*2}M^2\rangle(\theta) &= \int \mathrm{d}^2X_0 \cdots \int \mathrm{d}^2X_3 \prod_{i=0}^{3}\left(Q_\theta(|\boldsymbol{X}_i|)\right)\frac{\breve{X}_1^{*2}}{|\breve{X}_1|^2}\frac{\breve{X}_2^{*2}}{|\breve{X}_2|^2}\frac{\breve{X}_3^{\,2}}{|\breve{X}_3|^2}\frac{\breve{X}_4^{\,2}}{|\breve{X}_4|^2}\,\Gamma_5^{\mathrm{cart}}(\boldsymbol{X}_0-\boldsymbol{X}_1,\boldsymbol{X}_2-\boldsymbol{X}_0,\boldsymbol{X}_3-\boldsymbol{X}_0)\\ &= \frac{1}{(4\pi\theta^4)^4}\int \mathrm{d}^2\vartheta_1 \cdots \int \mathrm{d}^2\vartheta_3\,\Gamma_5^{\mathrm{cart}}(\boldsymbol{\vartheta}_1,\boldsymbol{\vartheta}_2,\boldsymbol{\vartheta}_3)\int \mathrm{d}Z\,Z\exp -\frac{4Z^2+\sum_{i=0}^{3}|\boldsymbol{q}_i|^2}{2\theta^2}\\ &\times\int \mathrm{d}\varphi_Z\,(\breve{Z}^*+\breve{q}_1^*)^2(\breve{Z}^*+\breve{q}_2^*)^2(\breve{Z}+\breve{q}_3)^2(\breve{Z}+\breve{q}_4)^2\\ &= \int \frac{\mathrm{d}\vartheta_1\,\vartheta_1}{\theta^2}\cdots\int\frac{\mathrm{d}\vartheta_3\,\vartheta_3}{\theta^2}\int\frac{\mathrm{d}\psi_{12}}{2\pi}\int\frac{\mathrm{d}\psi_{23}}{2\pi}K_5\left(\frac{\boldsymbol{q}_0}{\theta},\frac{\boldsymbol{q}_1}{\theta},\frac{\boldsymbol{q}_2}{\theta},\frac{\boldsymbol{q}_3}{\theta}\right)P_5^{\mathrm{cart},\times}(\boldsymbol{\vartheta}_1,\boldsymbol{\vartheta}_2,\boldsymbol{\vartheta}_3)\,\Gamma_5^{\times}(\vartheta_1,\vartheta_2,\vartheta_3,\psi_{12},\psi_{23}).\end{aligned} \tag{B.4}$$

A separation into E- and B-modes is possible following the prescription in Appendix A.3, with the explicit separation in Sect. 3.2.2.

B.2. Visual inspection of filters for fourth-order aperture statistics

In order to obtain insight into the shape and smoothness of the filters, the left panel in Fig. B.1 shows the filter for selected angular combinations. In both the case of symmetric angles (first two rows) and in a more general case, the profiles present substructure at a wide range of scales and a Gaussian decay at radii $\vartheta \gg \theta$.

The right panel in Fig. B.1 shows the angular dependence of the filters for two radial combinations. For large radii (first two rows) the filters K_i are peaked around $\psi_{12} = 0 = \psi_{23}$, while for $\vartheta_i \approx \theta$ the filters are smoother and alternate positive and negative.

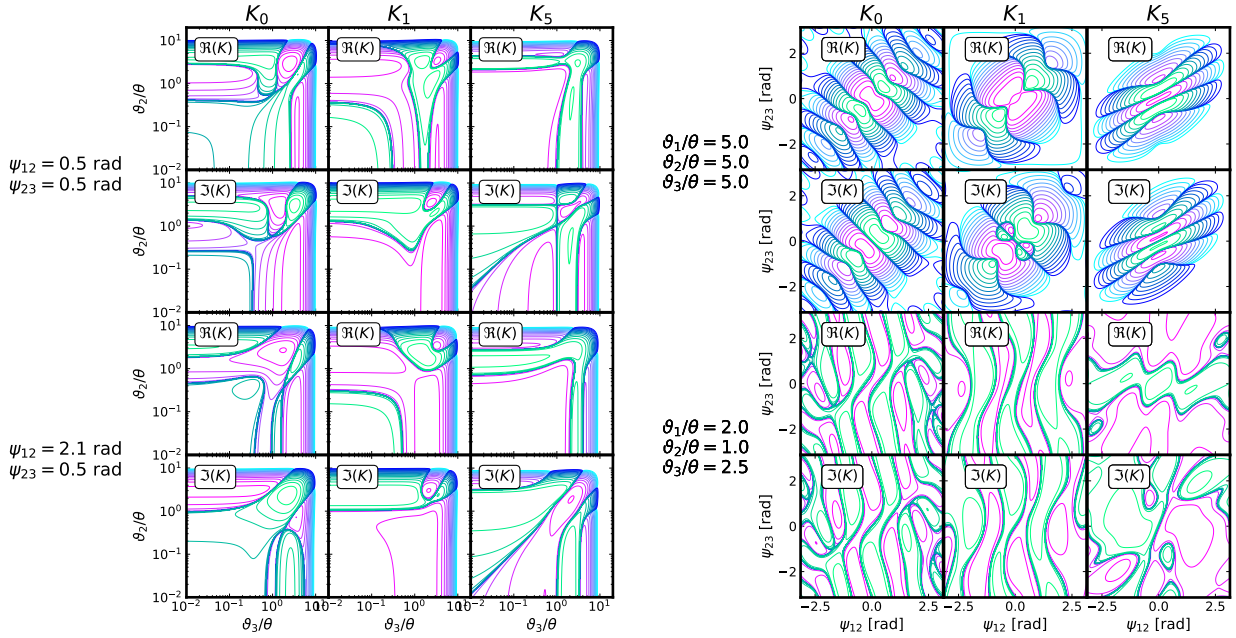

Fig. B.1. Filters for computing $\langle M^4\rangle(\theta)$, $\langle M^* M^3\rangle(\theta)$, and $\langle M^{*2} M^2\rangle(\theta)$ in terms of the 4PCF, as in Eq. (27); (Left) for given ψ_{12} and ψ_{23} combinations with the third radial variable fixed at $\vartheta_3 = \theta$ and (Right) for given radial combinations. Logarithmic contours with the minimum at 10^{-15} and a factor of five between them. Purple contours are positive values, green contours are negative ones.

Appendix C: Gaussian random fields: fourth-order statistics in terms of second-order statistics

C.1. Correlation functions

For a GRF the 4PCF only contains disconnected terms, so it can be split into a combination of 2PCF (Isserlis 1918)

$$\langle\gamma^{(*)}(\boldsymbol{X}_0)\gamma^{(*)}(\boldsymbol{X}_1)\gamma^{(*)}(\boldsymbol{X}_2)\gamma^{(*)}(\boldsymbol{X}_3)\rangle = \langle\gamma^{(*)}(\boldsymbol{X}_0)\gamma^{(*)}(\boldsymbol{X}_1)\rangle\langle\gamma^{(*)}(\boldsymbol{X}_2)\gamma^{(*)}(\boldsymbol{X}_3)\rangle + \langle\gamma^{(*)}(\boldsymbol{X}_0)\gamma^{(*)}(\boldsymbol{X}_2)\rangle\langle\gamma^{(*)}(\boldsymbol{X}_1)\gamma^{(*)}(\boldsymbol{X}_3)\rangle + \langle\gamma^{(*)}(\boldsymbol{X}_0)\gamma^{(*)}(\boldsymbol{X}_3)\rangle\langle\gamma^{(*)}(\boldsymbol{X}_1)\gamma^{(*)}(\boldsymbol{X}_2)\rangle, \tag{C.1}$$

where the shear on each point can be either conjugated or not. Every 2PCF can be expressed as

$$\langle\gamma(\boldsymbol{X})\gamma(\boldsymbol{X}+\boldsymbol{s})\rangle = \frac{\check{s}^4}{|\check{s}|^4}\left[\xi_-(|\check{s}|) + 2\mathrm{i}\xi_\times(|\check{s}|)\right], \qquad \langle\gamma(\boldsymbol{X})\gamma^*(\boldsymbol{X}+\boldsymbol{s})\rangle = \xi_+(|\check{s}|), \qquad \langle\gamma^*(\boldsymbol{X})\gamma^*(\boldsymbol{X}+\boldsymbol{s})\rangle = \frac{\check{s}^{*4}}{|\check{s}|^4}\left[\xi_-(|\check{s}|) - 2\mathrm{i}\xi_\times(|\check{s}|)\right] \tag{C.2}$$

with $\check{s}$ the complex number that represents the vector difference $\boldsymbol{s}$. For a field that does not violate parity $\xi_\times(|\check{s}|) = 0$ (Schneider et al. 2002). Here we explicitly keep $\xi_\times(|\check{s}|)$ for the sake of completeness.

In terms of the vectors $\boldsymbol{\vartheta}_i$ from Fig. 1 the fourth-order natural components are

$$\Gamma_0^{\mathrm{cart}}(\boldsymbol{\vartheta}_1,\boldsymbol{\vartheta}_2,\boldsymbol{\vartheta}_3) = \left(\frac{\check{\vartheta}_1}{|\check{\vartheta}_1|}\right)^4\left(\frac{\check{\vartheta}_3-\check{\vartheta}_2}{|\check{\vartheta}_3-\check{\vartheta}_2|}\right)^4 \xi_-(|\check{\vartheta}_1|)\,\xi_-(|\check{\vartheta}_3-\check{\vartheta}_2|) + \left(\frac{\check{\vartheta}_2}{|\check{\vartheta}_2|}\right)^4\left(\frac{\check{\vartheta}_3-\check{\vartheta}_1}{|\check{\vartheta}_3-\check{\vartheta}_1|}\right)^4 \xi_-(|\check{\vartheta}_2|)\,\xi_-(|\check{\vartheta}_3-\check{\vartheta}_1|) + \left(\frac{\check{\vartheta}_3}{|\check{\vartheta}_3|}\right)^4\left(\frac{\check{\vartheta}_2-\check{\vartheta}_1}{|\check{\vartheta}_2-\check{\vartheta}_1|}\right)^4 \xi_-(|\check{\vartheta}_3|)\,\xi_-(|\check{\vartheta}_2-\check{\vartheta}_1|), \tag{C.3}$$

$$\Gamma_1^{\mathrm{cart}}(\boldsymbol{\vartheta}_1,\boldsymbol{\vartheta}_2,\boldsymbol{\vartheta}_3) = \left(\frac{\check{\vartheta}_3-\check{\vartheta}_2}{|\check{\vartheta}_3-\check{\vartheta}_2|}\right)^4 \xi_+(|\check{\vartheta}_1|)\,\xi_-(|\check{\vartheta}_3-\check{\vartheta}_2|) + \left(\frac{\check{\vartheta}_3-\check{\vartheta}_1}{|\check{\vartheta}_3-\check{\vartheta}_1|}\right)^4 \xi_+(|\check{\vartheta}_2|)\,\xi_-(|\check{\vartheta}_3-\check{\vartheta}_1|) + \left(\frac{\check{\vartheta}_2-\check{\vartheta}_1}{|\check{\vartheta}_2-\check{\vartheta}_1|}\right)^4 \xi_+(|\check{\vartheta}_3|)\,\xi_-(|\check{\vartheta}_2-\check{\vartheta}_1|), \tag{C.4}$$

$$\Gamma_5^{\rm cart}(\boldsymbol{\vartheta}_1,\boldsymbol{\vartheta}_2,\boldsymbol{\vartheta}_3) = \left(\frac{\breve{\vartheta}_1^*}{|\breve{\vartheta}_1|}\right)^4 \left(\frac{\breve{\vartheta}_3-\breve{\vartheta}_2}{|\breve{\vartheta}_3-\breve{\vartheta}_2|}\right)^4 \xi_-(|\breve{\vartheta}_1|)\,\xi_-(|\breve{\vartheta}_3-\breve{\vartheta}_2|) \;+\; \xi_+(|\breve{\vartheta}_2|)\,\xi_+(|\breve{\vartheta}_3-\breve{\vartheta}_1|) \;+\; \xi_+(|\breve{\vartheta}_3|)\,\xi_+(|\breve{\vartheta}_2-\breve{\vartheta}_1|)\,. \tag{C.5}$$

The natural components $\Gamma_{2-4}^{\rm cart}$ can be obtained by renaming one of the vertices with a conjugated shear, for example $\Gamma_2^{\rm cart}(\breve{\vartheta}_1,\breve{\vartheta}_2,\breve{\vartheta}_3) = \Gamma_1^{\rm cart}(-\breve{\vartheta}_1,\breve{\vartheta}_2-\breve{\vartheta}_1,\breve{\vartheta}_3-\breve{\vartheta}_1)$. $\Gamma_{6-7}^{\rm cart}$, in turn, are equivalent to $\Gamma_5^{\rm cart}$ when renaming the second vertex with conjugated shear, for example $\Gamma_6^{\rm cart}(\breve{\vartheta}_1,\breve{\vartheta}_2,\breve{\vartheta}_3) = \Gamma_5^{\rm cart}(\breve{\vartheta}_2,\breve{\vartheta}_1,\breve{\vartheta}_3)$. This vertex exchange is an equivalent transformation to the one for the filters in Eq. (31).

These 4PCFs are finally converted to the × projection with the projector operators $P_l^{\times,\rm cart}$.

C.2. Aperture measures

We start here from the aperture measures as defined in Eq. (16), specifying to fourth-order and equal apertures.

For $\langle M^4\rangle(\theta)$, when substituting Eq. (C.1), we find three integrals, which are identical under permutation of the integration variable names $\boldsymbol{X}_0$ to $\boldsymbol{X}_3$. Moreover, the eight-dimensional integrals can be factorized into two four-dimensional ones, which are also identical to each other, giving

$$\langle M^4\rangle(\theta) = 3\left[\int \mathrm{d}^2X_0\, Q_\theta(|\boldsymbol{X}_0|)\int \mathrm{d}^2X_1\, Q_\theta(|\boldsymbol{X}_1|)\frac{\breve{X}_0^{*2}}{|\breve{X}_0|^2}\frac{\breve{X}_1^{*2}}{|\breve{X}_1|^2}\langle\gamma(\boldsymbol{X}_0)\gamma(\boldsymbol{X}_1)\rangle\right]^2 = 3\left[\int \frac{\mathrm{d}|\breve{s}||\breve{s}|}{\theta^2}\left(\xi_-(|\breve{s}|)+2\mathrm{i}\xi_\times(|\breve{s}|)\right)T_-\left(\frac{|\breve{s}|}{\theta}\right)\right]^2,$$

where in the last step we changed $\boldsymbol{X}_1 = \boldsymbol{X}_0 + \boldsymbol{s}$ and defined the functions T_- as in Jarvis et al. (2004), where in the derivation the cross term was implicitly set to zero. Therefore $\langle M^4\rangle(\theta) = 3[\langle M^2\rangle(\theta)]^2$.

For $\langle M^*M^3\rangle(\theta)$, when substituting Eq. (C.1), the three integrals are identical under permutation of the integration variable names $\boldsymbol{X}_1$ to $\boldsymbol{X}_3$ and the eight-dimensional integrals can be factorized into two four-dimensional ones, i.e.

$$\begin{aligned}\langle M^*M^3\rangle(\theta) &= 3\left[\int \mathrm{d}^2X_0\, Q_\theta(|\boldsymbol{X}_0|)\int \mathrm{d}^2X_1\, Q_\theta(|\boldsymbol{X}_1|)\frac{\breve{X}_0^{\ 2}}{|\breve{X}_0|^2}\frac{\breve{X}_1^{\ *2}}{|\breve{X}_1|^2}\langle\gamma^*(\boldsymbol{X}_0)\gamma(\boldsymbol{X}_1)\rangle\right]\\ &\times\left[\int \mathrm{d}^2X_2\, Q_\theta(|\boldsymbol{X}_2|)\int \mathrm{d}^2X_3\, Q_\theta(|\boldsymbol{X}_3|)\frac{\breve{X}_2^{\ *2}}{|\breve{X}_2|^2}\frac{\breve{X}_3^{\ *2}}{|\breve{X}_3|^2}\langle\gamma(\boldsymbol{X}_2)\gamma(\boldsymbol{X}_3)\rangle\right]\\ &= 3\left[\int \frac{\mathrm{d}|\breve{r}||\breve{r}|}{\theta^2}\xi_+(|\breve{r}|)T_+\left(\frac{|\breve{r}|}{\theta}\right)\right]\left[\int \frac{\mathrm{d}|\breve{s}||\breve{s}|}{\theta^2}\left[\xi_-(|\breve{s}|)+2\mathrm{i}\xi_\times(|\breve{s}|)\right]T_-\left(\frac{|\breve{s}|}{\theta}\right)\right],\end{aligned}$$

where we rewrote the variables $\boldsymbol{X}_1 = \boldsymbol{X}_0 + \boldsymbol{r}$ and $\boldsymbol{X}_3 = \boldsymbol{X}_2 + \boldsymbol{s}$, and defined T_+ as in Jarvis et al. (2004). Together, $\langle M^*M^3\rangle(\theta) = 3\left\langle M^2\right\rangle(\theta)\langle MM^*\rangle(\theta)$, and equivalent for the other aperture measures with one conjugated component.

Finally, for $\langle M^{*2}M^2\rangle(\theta)$ only two of the three integrals obtained when substituting Eq. (C.1) are identical under permutation of $\boldsymbol{X}_0$ and $\boldsymbol{X}_1$, or $\boldsymbol{X}_2$ and $\boldsymbol{X}_3$, giving

$$\begin{aligned}\langle M^{*2}M^2\rangle(\theta) =& 2\left[\int \mathrm{d}^2X_0\, Q_\theta(|\boldsymbol{X}_0|)\int \mathrm{d}^2X_2\, Q_\theta(|\boldsymbol{X}_2|)\frac{\breve{X}_0^{\ 2}}{|\breve{X}_0|^2}\frac{\breve{X}_2^{\ *2}}{|\breve{X}_2|^2}\langle\gamma^*(\boldsymbol{X}_0)\gamma(\boldsymbol{X}_2)\rangle\right]^2\\ &+\left\{\left[\int \mathrm{d}^2X_0\, Q_\theta(|\boldsymbol{X}_0|)\int \mathrm{d}^2X_1\, Q_\theta(|\boldsymbol{X}_1|)\frac{\breve{X}_0^{\ 2}}{|\breve{X}_0|^2}\frac{\breve{X}_1^{\ 2}}{|\breve{X}_1|^2}\langle\gamma^*(\boldsymbol{X}_0)\gamma^*(\boldsymbol{X}_1)\rangle\right]\right.\\ &\left.\times\left[\int \mathrm{d}^2X_2\, Q_\theta(|\boldsymbol{X}_2|)\int \mathrm{d}^2X_3\, Q_\theta(|\boldsymbol{X}_3|)\frac{\breve{X}_2^{\ *2}}{|\breve{X}_2|^2}\frac{\breve{X}_3^{\ *2}}{|\breve{X}_3|^2}\langle\gamma(\boldsymbol{X}_2)\gamma(\boldsymbol{X}_3)\rangle\right]\right\}\\ =& 2\left[\int \frac{\mathrm{d}|\breve{r}||\breve{r}|}{\theta^2}\xi_+(|\breve{r}|)T_+\left(\frac{|\breve{r}|}{\theta}\right)\right]^2 + \mathrm{Abs}\left(\int \frac{\mathrm{d}|\breve{s}||\breve{s}|}{\theta^2}\left(\xi_-(|\breve{s}|)+2i\xi_\times(|\breve{s}|)\right)T_-\left[\frac{|\breve{s}|}{\theta}\right]\right)^2,\end{aligned}$$

where we proceeded as in the previous cases and used that complex conjugation is distributive over addition and multiplication. Then $\langle M^{*2}M^2\rangle(\theta) = 2\left[\langle MM^*\rangle(\theta)\right]^2 + \mathrm{Abs}\left[\left\langle M^2\rangle(\theta)\right\rangle\right]^2$ and $\langle M^*MM^*M\rangle(\theta) = \left\langle M^*M^2M^*\right\rangle(\theta) = \left\langle M^{*2}M^2\right\rangle(\theta)$.

Appendix D: Estimation of derivatives from samples

D.1. Method

If we have access to a cosmological simulation suite with $i = \{1, \cdots, N_{\rm cosmo}\}$ distinct sets of cosmological parameters or samples, $\boldsymbol{\mu}^i$, we can measure an observable, $y = f(\boldsymbol{\mu})$, on the different cosmologies, $y^i = f(\boldsymbol{\mu}^i)$.[9] Here we approximate f by a first-order Taylor expansion around the fiducial values of the $N_{\rm param}$ parameters,

$$f(\boldsymbol{\mu}) = f|_{\rm fid} + \sum_{j=1}^{N_{\rm param}} \left.\frac{\partial f}{\partial \mu_j}\right|_{\rm fid} \left(\mu_j - \mu_{j,\rm fid}\right) + O(\boldsymbol{\mu} - \boldsymbol{\mu}_{\rm fid})^2 \tag{D.1}$$

$$\approx b + \sum_{j=1}^{N_{\rm param}} a_j \left(\mu_j - \mu_{j,\rm fid}\right); \tag{D.2}$$

$$f(\boldsymbol{\mu}^i) = b + \sum_{j=1}^{N_{\rm param}} a_j \left(\mu_j^i - \mu_{j,\rm fid}^i\right), \tag{D.3}$$

where in the first step we introduced the model parameters, a_j and b, and in the second step we specified for every sample cosmology. By defining the quantity $\boldsymbol{\mu}'^i = \left(\mu_1^i - \mu_{1,\rm fid}^i, \cdots, \mu_{N_{\rm param}}^i - \mu_{N_{\rm param},\rm fid}^i, 1\right)$ we can rewrite Eq. (D.3) as the linear combination

$$f(\boldsymbol{\mu}^i) = \sum_{j=1}^{N_{\rm param}+1} a_j' \mu_j'^i, \tag{D.4}$$

with model parameters $a_j' = a_j$ if $j \leq N_{\rm param}$ and $a_{N_{\rm param}+1}' = b$. The best-fit model parameters are such that they minimize the loss function,

$$\mathcal{L} = \sum_{i=1}^{N_{\rm cosmo}} w^i |y^i - f(\boldsymbol{\mu}^i)|^2, \quad \text{with} \tag{D.5}$$

$$w^i = \exp -\frac{1}{2\sigma^2} \left(\boldsymbol{\mu}^i - \boldsymbol{\mu}|_{\rm fid}\right)^{\rm T} \mathsf{C}_{\mu,\mu}^{-1} \left(\boldsymbol{\mu}^i - \boldsymbol{\mu}|_{\rm fid}\right), \tag{D.6}$$

where w^i is the weight of the i-th set of cosmological parameters. The w^i depend on the distance in cosmological parameter space to the the fiducial cosmology; on the covariance matrix of the cosmological parameters, $\mathsf{C}_{\mu,\mu}$, which is expected to be diagonal if the cosmologies are distributed on a latin hypercube, and can be computed from the set of cosmological parameters; and on the hyperparameter σ^2, the weighting scale. With w^i we give a higher weight to sets of cosmological parameters that are closer to the fiducial value, where the linear approximation for f is more accurate, but also more prone to noise.

The minimization of Eq. (D.5) w.r.t to the parameter a_k'

$$\frac{\partial \mathcal{L}}{\partial a_k'} = 0 \rightarrow \sum_{i=1}^{N_{\rm cosmo}} w^i y^i \mu_k'^i = \sum_{j=1}^{N_{\rm param}+1} \sum_{i=1}^{N_{\rm cosmo}} w^i \mu_k'^i \mu_j'^i a_j', \tag{D.7}$$

or in matrix formalism for all model parameters, defining $(M_w)_j^i = w^i \mu_j'^i$ and $(M)_j^i = \mu_j'^i$,

$$\boldsymbol{M_w}^T \boldsymbol{y} = \boldsymbol{M_w}^T \boldsymbol{M} \boldsymbol{a}' \rightarrow \boldsymbol{a}' = (\boldsymbol{M_w}^T \boldsymbol{M})^{-1} \boldsymbol{M_w}^T \boldsymbol{y}. \tag{D.8}$$

[9] We use upper indices to label each cosmological set and lower indices for the different cosmological parameters on each set.

From Eq. (D.2) we see that the partial derivatives are approximated by the first $N_{\rm param}$ components of the model parameters, $\boldsymbol{a}'$, while $a_{N_{\rm param}+1}'$ is an approximation of the observable at the fiducial cosmology.

Due to the construction of the weights, considering in the analysis a cosmological parameter on which the observables depend weakly, introduces noise in the derivatives w.r.t. all parameters. In such case, the derivatives w.r.t. the parameters with strong dependency can be made more stable by marginalizing over the noisy parameters.

D.2. Derivatives from the cosmo-SLICS ensemble

Since the derivatives only depend on one hyperparameter, σ, we can study the stability of the derivatives by inspecting their dependency on σ, considering `cSfid` as fiducial cosmology. From the cosmological parameters considered in *cosmo*-SLICS (cS19),[10] $\mu = \{\Omega_{\rm m}, S_8, h, w_0\}$, we marginalize over h and w_0, since we find that the non-tomographic aperture statistics on cS19 do not have enough constraining power to produce robust derivatives on such parameters.

The first two panels in Fig. D.1 show the derivatives of $\left\langle M_{\rm ap}^2 \right\rangle$, $\left\langle M_{\rm ap}^3 \right\rangle$, and $\left\langle M_{\rm ap}^4 \right\rangle_c$, with Jackknifing error bars over light cones and color coded by their weighting scale σ. For small σ only a few points contribute significantly, so the derivatives are biased toward the noisy estimate from a few cosmologies close to the fiducial value. The derivatives converge for increasing σ to the value we would recover if we set all weights to unity; therefore, they are here far from the linear approximation regime.

This study on σ is equivalent to investigating the case where the derivatives are only computed with the $A \leq N_{\rm cosmo}$ cosmologies closest to the fiducial cosmology, where we obtain convergence for $A > 18$ with $\sigma = 0.6$, and noise-dominated derivatives otherwise. The continuous nature of varying σ makes the noise for $\sigma < 0.6$ appear as a smooth bias in the derivatives.

For second- and third-order statistics we can compute the derivatives with finite differences from a theoretical model, with the values marked as blue rings in Fig. D.1.[11] Our method underestimates the derivatives by a degree that decreases for decreasing σ until the noise limit of $\sigma \approx 0.6$ in cS19.

We generated theoretical second- and third-order statistics that correspond to cosmological parameters close to `cSfid` in the $\{\sigma_8, \Omega_{\rm m}\}$ plane and used them to compute derivatives with the loss minimization method, recovering the theoretical derivatives from finite differences. The bias between the finite differences method and the loss minimization method in Fig. D.1 therefore arises from the sparsity of cS19 around `cSfid` and the linearity assumption from Eq. (D.3). With these theoretical (noiseless) points close to `cSfid` we find the best results for a combination of $N_{\rm cosmo} < 25$ and $\sigma \ll 1$. When studying only cS19, such combinations are dominated by noise, so we proceed with $N_{\rm cosmo} = 25$, $\sigma = 0.6$.

The third panel in Fig. D.1 shows the predicted value of the observable, b, along with the value measured on `cSfid` (in black) and the theoretical model for second- and third-order

[10] From the 26 sets of cosmological parameters available, each one of them with 25 lightcones, we discard the third light cone, as one of the redshift slices has a significant $\langle M_{\rm ap} \rangle \neq 0$ and discarding only such map would change the $n(z)$.

[11] We compute second-order statistics from the nonlinear cold-dark-matter BACCO emulator (Angulo et al. 2021) and `pyccl` (Chisari et al. 2019) and third-order statistic from the cold-dark-matter BiHalofit (Takahashi et al. 2021).

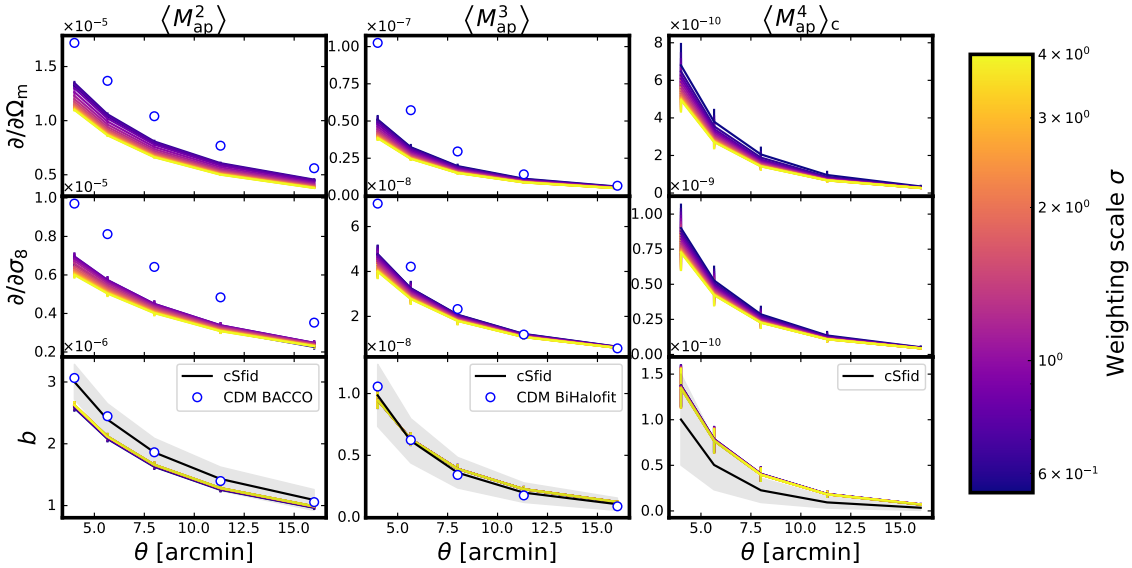

Fig. D.1. Stability of the model parameters for the derivatives when varying the weighting scale σ (see Eq. (D.6)). All points have error bars from Jackknifing over light cones. The first two rows correspond to the derivatives with respect to the cosmological parameters and the third one to the model prediction for the given order of the aperture statistics. Blue rings mark the values obtained from theory for the aperture statistics and their derivatives, estimated from finite differences. The agreement between b and the measurement in `cSfid` (black) is a test of the robustness of the method.

statistics (blue rings). We find that, with our method, we predict a value of the observables that is compatible within 1σ to the one measured in `cSfid`. We attribute the difference in second- and fourth-order statistics to the slight changes in redshift distribution for the different cS19 cosmological sets, arising from the varying number of convergence maps for each set. Moreover, neighboring aperture scales are highly correlated, which is not considered in the Jackknifing error bars nor in the 1σ region from `cSfid`.

In summary, we find that derivatives are stable when considering the cosmological parameters Ω_m and σ_8 and marginalizing over h and w_0, but become unstable if we try to constrain all four parameters simultaneously. When using sparse simulations around the fiducial value, as cS19 around `cSfid`, the derivatives are biased toward lower values, resulting in overestimated Fisher ellipses for the independent aperture statistics, and possibly under- or overestimated for the joint analysis. Even on such sparse simulations, we recover a value of the mean for second- and third-order statistics compatible within their 1σ precision to the measured one.

D.3. Stability of the ellipses

Fisher ellipses are fully described by two quantities, i.e. a direction and an area. For the two-dimensional distribution of the i-th and the j-th parameters, these quantities can be the Pearson correlation coefficient,

$$p_{i,j} = \frac{C_{i,j}}{\sqrt{C_{i,i}C_{j,j}}}, \tag{D.9}$$

with $C = F^{-1}$ and F the Fisher matrix, and the Figure of Merit of order n,

$$\mathrm{FoM}_{i,j} = \left[2\pi n^2 \left(C_{i,i} + C_{j,j}\right) \sqrt{1 - p_{i,j}^2}\right]^{-1}, \tag{D.10}$$

which is the inverse of the area of the ellipse enclosing the $n\sigma$ region, where here $n = 1$.

The left panel in Fig. D.2 shows the stability of p and the FoM when varying the number of cosmologies considered for the derivatives or the weighting scale. When using too few cosmologies, or $\sigma < 0.6$, we do not capture enough information, and the ellipses are noise-dominated. The horizontal lines, using all $N_{\mathrm{cosmo}} = 25$ and $\sigma = 0.6$, are the values used for the Fisher forecast. p and the FoM are compatible within their Jackknifing error bars for $\{\langle M_{ap}^2\rangle, \langle M_{ap}^3\rangle\}$ and $\{\langle M_{ap}^2\rangle, \langle M_{ap}^3\rangle, \langle M_{ap}^4\rangle_c\}$, so we do not report a significant improvement when including fourth-order statistics, as discussed in Sect. 5.2.

The right panel in Fig. D.2 shows the equivalent analysis on the $\{\Omega_m, \sigma_8\}$ ellipse, when we do not marginalize over h and w_0 in the computation of the derivatives. The FoM is around an order of magnitude smaller, sign that we cannot constrain all four cosmological parameters. Albeit noise-dominated, we find the strongest change for fourth-order statistics, hinting at a stronger dependency of fourth-order statistics on h and w_0.

Further tests for the accuracy of the FoM and other derived quantities from Fisher forecasts were developed in for example, Euclid Collaboration: Blanchard et al. (2020) and Yahia-Cherif et al. (2021) to meet the requirements of the upcoming Stage IV surveys. Yahia-Cherif et al. (2021) determine the required accuracy on the elements of the Fisher matrix with a perturbation-based approach, in order to retrieve a given level of precision of the FoM, while Euclid Collaboration: Blanchard et al. (2020) do so by propagating the uncertainty on the Fisher elements to the FoM and orientation of the ellipses. These tests rely on the possibility to arbitrarily increase the accuracy on the Fisher elements i.e. by obtaining more precise derivatives, thus requiring an analytical model for the given statistical measure or a denser set of cosmological simulations.

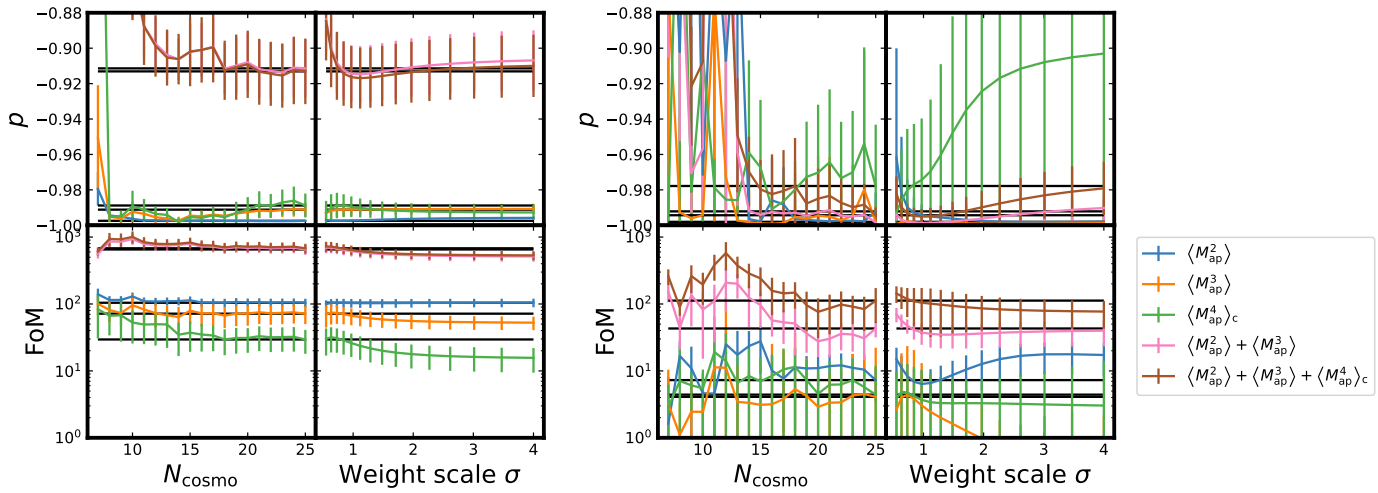

Fig. D.2. Stability of the $\{\Omega_{\rm m}, \sigma_8\}$ Fisher ellipses when varying the number of cosmologies around the fiducial value, $N_{\rm cosmo}$, or the weighting scale, σ; specified through the Pearson correlation coefficient p, measure of the orientation of the ellipse, and the Figure of Merit FoM, measure of the area of the ellipse. The different colors correspond to the given combination of order for the aperture statistics considered in the analysis. Comparison of the results when marginalizing over h and w_0 in the computation of the ellipses (Left), with stable ellipses; and the results when we try to constrain all cosmological parameters from cS19 (Right), where projection effects from the unconstrained parameters make the ellipses unstable.